Sedimentary Geology 446 (2023) 106340

Contents lists available at ScienceDirect

Sedimentary Geology

journal homepage: www.elsevier.com/locate/sedgeo

Comparison of three grain size measuring methods applied to coarse-grained gravel deposits

Philippos Garefalakis [a,*], Ariel Henrique do Prado [a], David Mair [a], Guilhem Amin Douillet [a], Franziska Nyffenegger [b], Fritz Schlunegger [a]

[a] University of Bern, Institute of Geological Sciences, Baltzerstrasse 1+3, 3012 Bern, Switzerland
[b] Berner Fachhochschule (BFH), Institut für Siedlungsentwicklung und Infrastruktur ISI, Kompetenzbereich Geotechnik und Naturereignisse, Pestalozzistrasse 20, 3400 Burgdorf, Switzerland

ARTICLE INFO

Article history:
Received 11 October 2022
Received in revised form 27 January 2023
Accepted 28 January 2023
Available online 4 February 2023

Editor: Dr. Brian Jones

Keywords:
Grain size
Photo-based grain size measurement
Gravel
Conglomerate
Sedimentary rocks

ABSTRACT

The size of grains in gravel and conglomerate deposits is most easily measured on photos taken from related outcrops. However, the occlusion of grains by the sedimentary matrix or other grains, and possible distortions of photos, could introduce a bias in such datasets. Here, we explore the uncertainties associated with datasets where the lengths of the grains were measured on photos. To this end, we analysed coarse-grained (>2 mm) fluvial material from a gravel pit (Bern, Switzerland). We compared grain size data collected from digital photos with the results where the same material was measured with a calliper and mechanically sieved. Our analyses reveal that the percentile values such as the D_{16}, D_{50} and D_{84} of datasets where the grains' longest visible axes were measured on digital photos best correlate to the corresponding percentile values of data collected through sieving. We also find that the longest visible axes of grains measured on digital photos are c. 17 % smaller than the lengths of the intermediate *b*-axes of grains measured with a calliper. We therefore suggest to measure the longest visible axes on digital photos, and to correct the data by a corresponding factor such as +17 % for the target grain size percentiles.

1. Introduction

Grain size distributions, percentiles values thereof and grain shapes are essential to quantify the dynamics and processes of sediment transport in rivers (e.g., Dade and Friend, 1998; Church, 2006; Petit et al., 2015). Grain size distributions additionally allow a classification of the sorting of a grain assemblage (e.g., Inman, 1952; Rice and Church, 2010; Schlunegger et al., 2020) and help to characterize the morphologies and bedforms of coarse-grained fluvial deposits (e.g., Lane, 1955; Brayshaw, 1984; Leopold, 1992; MacKenzie et al., 2018). Research in these fields has mainly focussed on material >2 mm, which is commonly referred to as the 'coarse-grained fraction' of the clastic material, and called gravel or conglomerate for unconsolidated or lithified material, respectively (Wentworth, 1922). Fluvial transport of such material starts if a grain-size dependent flow strength is exceeded, and the subsequent transport occurs as bedload through rolling and/or gliding along the riverbed (e.g., Dade and Friend, 1998; Recking, 2010). The transport of smaller grains (<2 mm, sand fraction and finer) either occurs as bedload or suspension load, depending on the strength and dynamics of the flow (e.g., Parker, 1990; Wong and Parker, 2006).

A single grain can be described as an ellipsoid, where its three axes, the largest-, the intermediate- and the smallest-axis (all oriented perpendicular to each other) are referred to the *a*-, *b*- and *c*-axis, respectively (Yuzyk and Winkler, 1991; Fig. 1a). The ratio of these individual grain axes allows for a quantitative characterisation of the grain shape (Zingg, 1935; Blott and Pye, 2007). From the three axes of a grain, the *a*-axis is generally oriented sub-perpendicular to the water flow direction whereas its orthogonal *b*-axis is aligned sub-parallel and the *c*-axis vertical to the discharge direction (Wadell, 1936; Brayshaw, 1984; Aberle and Nikora, 2006; Fig. 1a). Consequently, the *b*-axis is generally used for the calibration of hydraulic formulae elaborated from flume experiments and for the quantification of sediment fluxes (e.g., Meyer-Peter and Müller, 1948; Parker, 1990; Recking, 2013).

1.1. Challenges with measuring grains from outcrops and scope of the study

Most authors investigating the sizes and shapes of coarse-grained material have focused on modern systems where individual grains are lying flat on gravel bars and where the *a*−/*b*-axes plane can be viewed

Abbreviations: LVA, Longest visible axis; *SVA*, Shortest visible axis.

* Corresponding author.
E-mail address: philippos.garefalakis@geo.unibe.ch (P. Garefalakis).

https://doi.org/10.1016/j.sedgeo.2023.106340

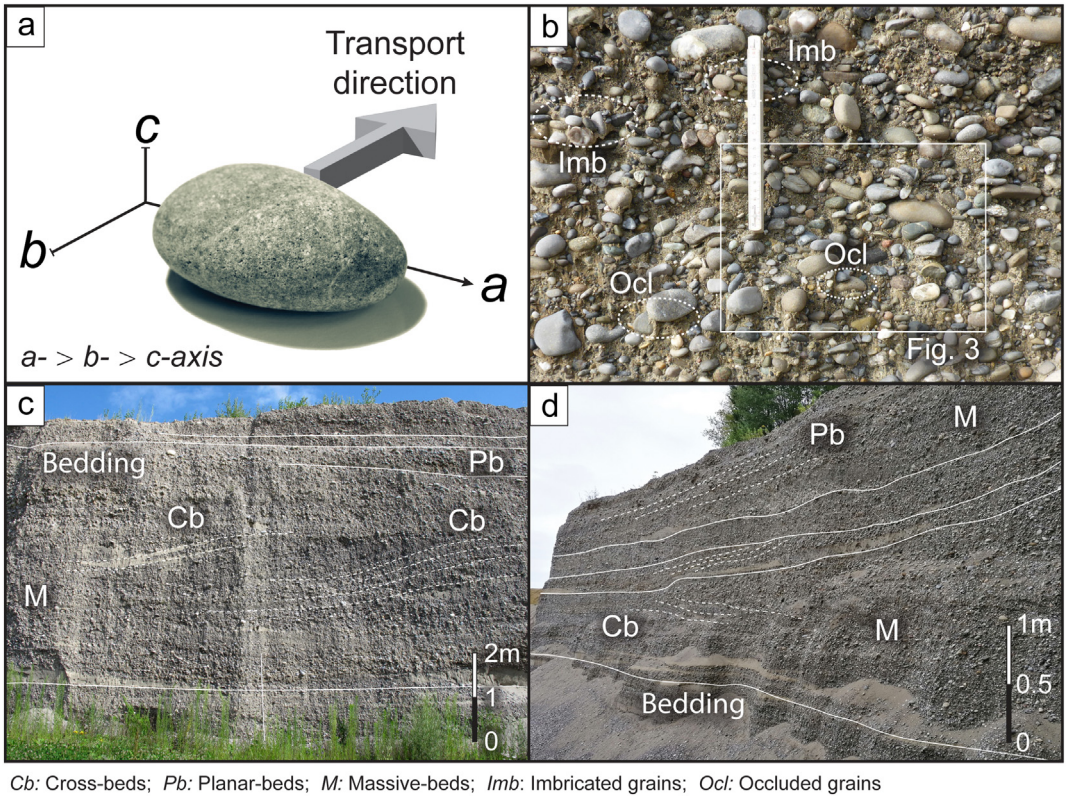

Fig. 1. Grain axes and coarse-grained gravelly outcrops: a) Grain axes in relation to each other and to the transport direction. b) Close-up image of a gravel outcrop (location 3; Fig. 2a) where imbricated and occluded grains are visible. c) and d) Example of outcrops with bedding surfaces perpendicular to the wall exposure. Occasionally, cross-, parallel- and massive-bedded structures are visible. See also Fig. 2 for location of these outcrops. Photo c) © N. Akçar / J. Pfander, 2020.

from above (Johansson, 1976; Brayshaw, 1984; Strom et al., 2010). However, the partial hiding of clasts due to imbrication or burial of individual grains poses major challenges when collecting grain size data from photos (e.g., Kellerhals and Bray, 1971; Adams, 1979; Graham et al., 2010). Furthermore, since photos display the grains as projections in 2D, they cannot resolve the full 3D-view of a single grain, which introduces an additional bias during the collection of such grain size datasets (e.g., Warrick et al., 2009; Stähly et al., 2017). This problem is amplified for photos taken from deposits of ancient fluvial systems like unconsolidated gravel or consolidated conglomerate beds, because larger grains might partially occlude neighbouring clasts, or the fine-grained matrix can hide parts of individual clasts. Such archives are commonly exposed through outcrops (Fig. 1), which cut (sub)-vertically through the bedding, thus exposing the thickness of a layer rather than the surface of a bed. Outcrops thus tend to display the *a*-and *c*- or the *b*- and *c*-axes (rather than the *a*- and *b*-axes when seen from above), which in turn depends on the paleoflow direction (Paola and Mohrig, 1996; Storz-Peretz and Laronne, 2013; Guerit et al., 2018). The entire length of a grain can thus only be seen if the material is completely excavated and measured with a calliper. Accordingly, the identification and measurement of specific grain axes (e.g., the *b*-axis), have remained a challenge.

Here, we address this problem and explore the uncertainties that can be associated upon collecting grain size datasets from outcrops of gravelly deposits. For this, we compare the percentile values of datasets where the grains were measured (i) by hand with a calliper, (ii) on digital photos and (iii) through sieving of the same material. Among the three methods, the presumably simplest, non-invasive, and least time-consuming one is the approach where the grains are measured on digital photos. We therefore put our major focus on the results of photo surveys and explore whether photo-specific factors (distorted or non-distorted, rectified photos), different approaches to select the grains on photos (either randomly or using a regular spaced grid), and the number of measurements introduce a bias upon collecting grain size datasets.

2. Previous studies

2.1. Measuring grains from gravelly riverbeds

Over the past decades, the quantification of coarse material in modern streams has undergone a significant development. Time-consuming in-situ class counting (e.g., Wolman, 1954) and sieving techniques (e.g., Batel, 1960) were partially substituted by manual collections of grain size datasets on photos (e.g., Ritter and Helley, 1969; Kellerhals and Bray, 1971; Adams, 1979) and approaches where clasts were semi-automatically measured (e.g., Butler et al., 2001; Buscombe, 2008; Graham et al., 2010; Purinton and Bookhagen, 2019). Grain measurements on photos (both manually or semi-automatic) are usually accomplished on a selection of grains only, using either grid-by-area (e.g., Ibbeken and Schleyer, 1986; Church et al., 1987) or grid-by-number concepts (i.e., class-based; e.g., Wolman, 1954; Kellerhals and Bray, 1971). Nowadays the flourishing use of uncrewed aerial vehicles (i.e., drones) allows simple and rapid surveys of large areas. This has proven an efficient method for the quantification of grain sizes (e.g., Carbonneau et al., 2018; Woodget et al., 2018; Marchetti et al., 2022). In the past years, applications of semi-automatic grain size measuring methods, where algorithms model ellipsoids around single grains, have gained an increasing popularity (Detert and Weitbrecht, 2012; Purinton and Bookhagen, 2019). Despite improvements in such techniques, measuring sizes of fluvial gravels in an accurate and reproducible way still bears challenges (e.g., Chardon et al., 2021; Purinton and Bookhagen, 2021; Mair et al., 2022).

2.2. Measuring grains from outcrops of sedimentary rocks

Sieving has been used to determine grain sizes from coarse-grained unconsolidated material (e.g., Claude et al., 2017; Preusser et al., 2021). It avoids selective picking of clasts, yet it delivers a single mesh-size value averaging a 3-parameter shape. Other attempts to measure grain sizes from such deposits were accomplished after the clasts were excavated from the outcrops. Individual grains were then measured manually with the help of callipers. However, this method is time consuming, yields a limited number of measurements, and bears the risk of shattering individual pebbles upon extraction, (Tanner, 1944; Haldemann, 1948; Nemec et al., 1980). Subsequently, the measurement of grains on photos has attracted interest because this has proven a simple, non-invasive, and least time-consuming method. This is especially the case when the deposits are lithified (such as conglomerate beds) and individual clasts cannot be readily extracted. Neumann-Mahlkau (1967) were among the first to conduct such surveys applied to outcrops. They particularly found that measuring the grains' longest visible axes on photos yield different results (differences of ±10–50 %) than sieving the same material. Based on this work, the grains' longest visible axes have been preferably measured on photos taken from outcrops (e.g., Paola and Mohrig, 1996; Duller et al., 2010; Litty et al., 2016; Garefalakis and Schlunegger, 2018). Similarly, upon using material collected from a 1.2 m-deep trench in a gravel bed, Guerit et al. (2018) evidenced differences (±10–15 %) between grain size data that was collected through sieving the material or through measuring the length of the *b*-axis by hand and calliper. In other contributions, Graham et al. (2005a, 2005b) introduced what they referred to as an automatic grain sizing (AGS) technique where the shape of individual grains (visible on photos) is automatically fitted through ellipsoids. These were then used to establish a grain size dataset. Such an approach yields area-by-number results, and the data needs to be converted following e.g., Kellerhals and Bray (1971). Storz-Peretz and Laronne (2013) built on this AGS method and found agreements ranging from ±3 to ±27 % (values are method specific) between the results where grains were measured on photos, by hand and with a calliper after excavation of the material, and finally through sieving the material.

Storz-Peretz and Laronne (2013) showed that shaded photos taken from short distances provided better data than photos taken with either a flash or a strong exposure contrast. For volcaniclastic sediments, Smith and Maxwell (2021) applied photogrammetric techniques on photos taken with drones, on which they measured the longest and shortest visible axes of grains >2 cm with a workflow fully applicable to coarse-grained fluvial successions.

3. Study site and methods

3.1. Study site

The study was realised in the Finsterhennen gravel pit (approx. 47°00′55″N/7°10′10″E; Bern, Switzerland) where unconsolidated coarse-grained fluvial material is exposed in large headwalls (Fig. 2). For these Quaternary deposits, measurements of cross-bed orientations and alignments of imbricated clasts revealed a paleoflow direction towards the N-NE (Fig. 2a; Pfander et al., 2022). We collected grain size data from eight locations that have four different orientations relative to the paleoflow direction (Fig. 2a). The grain size data from these locations were grouped as pairs (hereafter sites A – D), where sites A and C are oriented sub-perpendicular to the paleoflow, whereas sites B and D are aligned sub-parallel to the measured paleoflow direction (Fig. 2a and b). All clasts were extracted from the same c. 7 m-thick stratigraphic layer (i.e., FIH-S – LFA 4 in Pfander et al., 2022). The analysed deposits comprise clast-supported coarse-grained gravels, which are mostly massive-bedded but show cross-beds and imbrications in places (Fig. 1b, c and d). The grains consist of a large variety of lithologies, mostly derived from Alpine conglomerates, with a predominant occurrence of limestone constituents and a minor contribution of quartzites, granites and metamorphic pebbles (Pfander et al., 2022).

3.2. Data collection

In the field, we first sprayed an outcrop surface spanning c. 0.5–1 m^2 using a biodegradable yellow paint for later identification of the grains. We then took digital photos with a hand-held camera (Panasonic Lumix FT5, digital single lens mirrorless camera, 16.6 megapixels, JPEG-photos of format 4:3). By taking photos at a distance of 1–1.5 m from the outcrops, enough (> 200) clasts are portrayed on one single photo, and the photo resolution is sufficient to allow identification of grains ≥2 mm (e.g., Storz-Peretz and Laronne, 2013). We took photos perpendicular to the outcrop to avoid perspective distortion effects. We then measured only grains situated approximately 10 cm away from the photo frame to reduce distortion introduced by the camera lens. Nevertheless, we measured grains on the original (distorted) and the ortho-corrected (undistorted) photos to explore whether this influences the resulting grain size datasets. The related orthorectification was accomplished using the method of Zhang (2000), which is implemented in *OpenCV* (Bradski, 2000). The resolution of the distorted and undistorted photos is quite similar and ranges between 0.14 and 0.29 mm/pixel. Next, the material was excavated with a shovel at a depth of approximately twice the size of the largest visible grain, and the material, which also includes the fines <2 mm and grains beyond the coloured surface, was collected in a tarpaulin to prevent any loss of coloured grains. We measured only the coloured grains (that are equally visible on the photos) by hand with a calliper, and we sieved the bulk-material (fines <2 mm included) in the laboratory. Hereafter, the results of the manual measurements with the help of a calliper are referred to as hand data, the datasets collected on photos as photo data and the datasets established through sieving as sieve data, respectively.

For each site A – D, individual samples from two neighbouring outcrop locations were merged so that the material composition of the sampled outcrop was better represented (Mosley and Tindale, 1985). We then measured 200 grains per sample site upon collecting the data by hand and calliper and on photos. This number is sufficient to calculate accurate percentile values for moderately- to well-sorted material (Daniels and McCusker, 2010; Galia et al., 2017; Eaton et al., 2019), as is the case in the Finsterhennen gravel pit (Pfander et al., 2022). Upon sieving, the minimum representative weight of the sample to be collected was estimated based on the length of the largest *b*-axis measured with a calliper. Ideally, as documented in the tables by various authors (e.g., Neumann-Mahlkau, 1967; Church et al., 1987; Bunte and Abt, 2001), the percentage of the largest grains should be 1 % of the sampled bulk-material if the lengths of the *b*-axis lays between 32 and 128 mm. However, in case where this length is larger than 128 mm, the largest grains could constitute 5 % to the sample mass (Church et al., 1987; Bunte and Abt, 2001; Attal et al., 2015). At each sample site (Fig. 2a) we excavated between 32 and 61 kg of bulk-sediment (Table 1) and yielded corresponding values between approximately 0.4–5.5 %. Although these (e.g., site A; Table 1) are in cases slightly larger than suggested for an ideal survey (Church et al., 1987), they can be regarded as acceptable (Guerit et al., 2018; Watkins et al., 2020; Harvey et al., 2022). Note that grains <2 mm were then removed from the datasets for further analyses to ensure a consistent comparison between the different measuring methods, because grains <2 mm cannot be measured by hand with callipers and are barely detectable on photos taken with the setup (camera, distance) used in this study.

3.3. Grain size measurement protocols

3.3.1. Measurements by hand and calliper

For the collection of the hand data (Table 2), the coloured grains were separated from the others, evenly poured on a tarpaulin, and we blindly picked grains for measuring the lengths of the *a*-, *b*- and *c*-axis

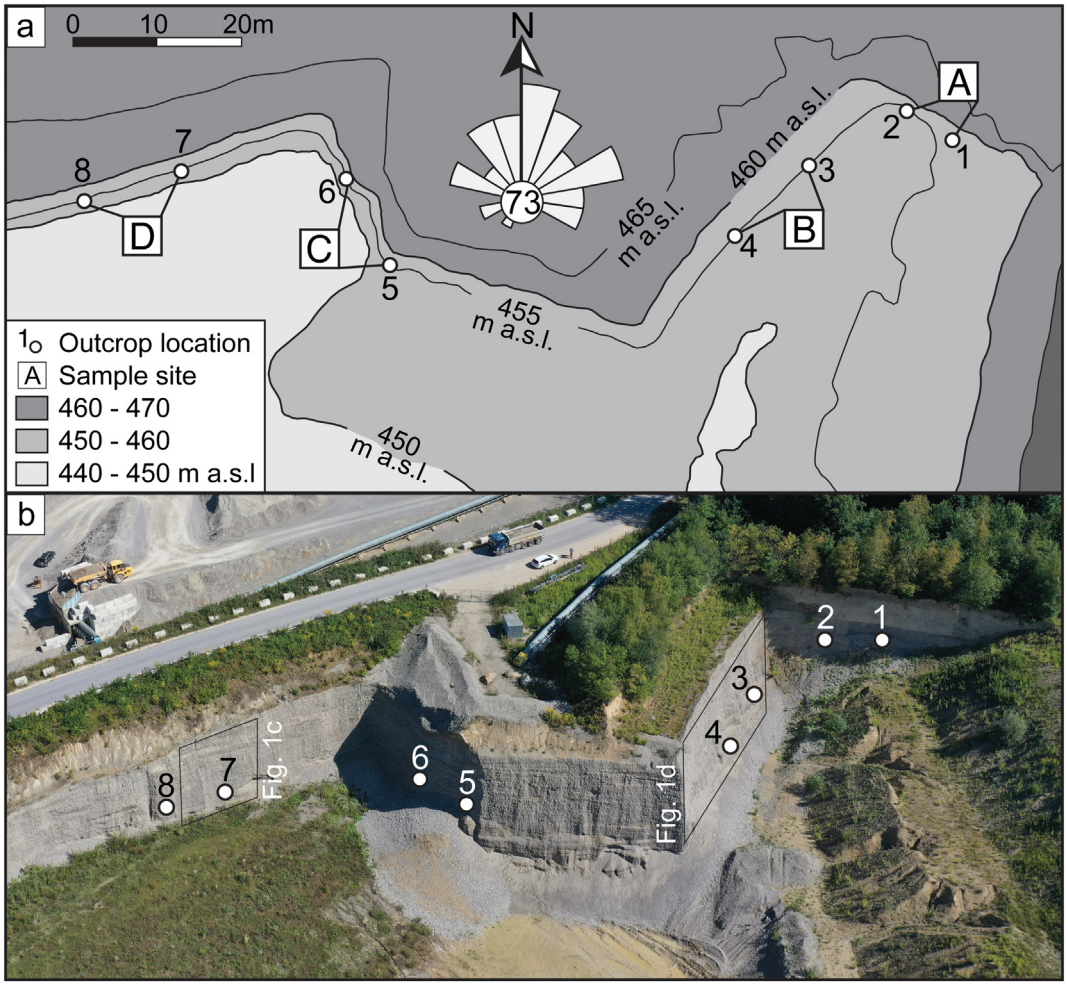

Fig. 2. Study site: a) Contour map of the gravel pit near Finsterhennen (Bern, Switzerland) with locations 1–8 and sample sites A-D (© Swisstopo). Discharge rose mod. After Pfander et al., 2022. b) Drone-photo showing the gravel pit with locations 1–8 and outcrops of Fig. 1. Photo b) © N. Akçar / J. Pfander, 2020.

with a digital calliper (resolution of 0.01 mm and precision of ±0.03 mm). Two grains larger >150 mm (*a*-axis) from site A were measured with a meter stick, yet at a lower precision (c. ±5 mm).

3.3.2. Measurements on digital photos

On each photo, we manually measured the longest visible axis (hereafter denoted as *LVA*) and the shortest visible axis (hereafter denoted as *SVA*), which are oriented perpendicular to each other. We followed two approaches upon selecting the grains to be measured (Table 2): A digital grid was added on each photograph as a first approach (grid-approach, *GA*; Fig. 3a); and randomly placed dots were generated on each photo as a second one (random-approach, *RA*; Fig. 3b). For the *GA* (e.g., Green, 2003; Warrick et al., 2009; Strom et al., 2010), we placed a regularly spaced grid of 4 × 4 cm calibrated to the meter stick on each photo (Fig. 3a). The grid size has been selected using the average grain size of c. 39 mm of the hand data (*a*-axis) of all 4 sample sites, which varies between 31.5 mm (site B) and 48.9 mm (site A). Following this method, we measured the *LVA* and *SVA* of each grain situated beneath an interception dot (Fig. 3a). The *RA* is a method where the *LVA* and *SVA* of coincidentally marked grains are measured (e.g., Wolman, 1954; Duller et al., 2010; Whittaker et al., 2011; Fig. 3b). Such a selection of grains is accomplished through superimposing randomly generated dots on the photos using a built-in ImageJ Macro (vs. 1.51f; Rasband, 1997-2018). In cases where the same grain was situated beneath multiple grid-intersection dots (*GA*) or several randomly placed dots (*RA*), this grain was measured only once. This approach is thought to reduce a potential bias caused by an overrepresentation of large grains (Diplas and Fripp, 1992; Bunte and Abt, 2001; Attal et al., 2015), but is different from other but similar grid-based measuring methods (e.g., Kellerhals and Bray, 1971). Additionally, both methods (*GA* and *RA*) were shown to yield consistent results, and they prevent a selective bias by the operator (e.g., Kellerhals and Bray, 1971; Adams, 1979; Ibbeken and Schleyer, 1986; Church et al., 1987; Strom et al., 2010). Following the aforementioned concepts, we manually measured a total of 100 grains per photo (i.e., 200 measurements per site) with the photo analysis software ImageJ. This resulted in four grain size datasets for each location, which are referred to as: *GAD* (grid-approach distorted photos), *GAU* (grid-approach undistorted photos), *RAD* (random-approach distorted photos) and *RAU* (random-approach undistorted photos), respectively (Table 2).

Table 1
Sieve sample mass: Bulk-weight and truncated-weight (rounded to 2 decimals) of the sieve samples for each sample site.

Sieve data	Site A	Site B	Site C	Site D
Bulk samples [kg]	61.38	32.96	37.41	40.09
Used samples [kg]	50.14	25.08	30.59	31.10
Fines < 2 mm [kg]	11.24	7.88	6.82	8.99
Fines < 2 mm [%]	18.31	23.91	18.23	22.42
Largest *b*-axis (hand data) [mm]	139.93	47.43	69.01	68.32
Approx. proportion of largest *b*-axis to bulk samples[a] [%]	5.1	0.4	1.3	1.2
Approx. proportion of largest *b*-axis to used samples[a] [%]	5.5	0.6	1.6	1.6

[a] After Church et al., 1987.

Table 2
Grain size measuring approaches: Key properties of the methods used in this study.

Method name	Measuring approach	Specific factor	Axes	Sample size	References (selection)
Hand	Measurement by calliper	Grains >150 mm by meter-stick	*a*-/*b*-/*c*-axis	200	Wolman, 1954 Green, 2003
Photo	*GAD*: measurement beneath grid-intersection	Distorted images	*LVA*/*SVA*	200	Kellerhals and Bray, 1971
Photo	*GAU*: measurement beneath grid-intersection	Non-distorted images	*LVA*/*SVA*	200	Ibbeken and Schleyer, 1986
Photo	*RAD*: measurement when marked by random dot	Distorted images	*LVA*/*SVA*	200	Paola and Mohrig, 1996
Photo	*RAU*: measurement when marked by random dot	Non-distorted images	*LVA*/*SVA*	200	Bunte and Abt, 2001 Rice and Church, 2010
Sieving	Dry-/wet-sieving	Weight-percentage; square-hole sieves	*Ds*[a] (*b*-axis equiv.)	30–60 kg[b]	Church et al., 1987 Attal et al., 2015

LVA: Longest; and ***SVA***: Shortest visible axis. ***GAD***: Grid-approach, distorted images; ***GAU***: Grid-approach, undistorted images. ***RAD***: Random-approach, distorted images; ***RAU***: Random-approach, undistorted images.
[a] *Ds*: sieve-axis; Square-hole sieves allow the *b*-axis of a grain to pass through (e.g., Church et al., 1987).
[b] Sampling weight depending on proportion of the largest *b*-axis from the hand data to the sampled mass (see also Table 1).

3.3.3. Sieving of the material

The mechanical dry- (fraction >0.5 mm) and wet-sieving (fraction <0.5 mm) of the sediment was performed in a laboratory (Berner Fachhochschule, Switzerland) following SN EN-standards (SN EN 933-1/2012-03; Table 2). The dry-sieving was effectuated with a Haver EML 400 Digital Plus sieve shaker (Haver and Boecker OHG) with square-hole sieves (mesh sizes from 0.5 to 125 mm, with intervals of doubling each mesh size). Grains >125 mm were measured separately with a meter stick (*b*-axis), weighted, and assigned to the grain size class 125–250 mm. The wet-sieving was performed using a Retsch AS 200 sieve shaker (Retsch GmbH; sieve mesh sizes of 0.063 mm, 0.125 mm and 0.250 mm). This was accomplished on a homogenised sub-sample of 50 g that was previously separated from the <0.5 mm fraction. For the sieve data, the sieve mesh sizes (or sieve bin-openings) are thought to represent the length of the *b*-axis, because square-hole sieves allow in general individual grains with this specific axis to pass through (Church et al., 1987; Stähly et al., 2017). Therefore, the sizes of the percentile values are hereafter denoted as the sieve-axis.

3.4. Limitations and biases related to the three measuring methods

3.4.1. Measuring grains with a calliper

Measuring by hand and calliper involves the risk of a selective bias and under-sampling (e.g., Fripp and Diplas, 1993; Marcus et al., 1995; Wohl et al., 1996; Galia et al., 2017), and it may yield less precise results for large, small, or irregular-shaped grains (Fripp and Diplas, 1993; Marcus et al., 1995). Additionally, the shape of grains can lead to a misidentification of a specific axis, e.g., for rounded or spherical grains that might have similar long axes (Yuzyk and Winkler, 1991). Because we measured all three grain axes, we tested whether the resulting grain sizes, using the hand *b*-axes as a reference, depend on the grain shape. For this, we classified the hand data into four shape endmembers (Zingg, 1935; Blott and Pye, 2007) referred to as: flat if *b*-/*a*-axes ≥2/3 and *c*-/*b*-axes <2/3; spherical if *b*-/*a*-axes ≥2/3 and *c*-/*b*-axes ≥2/3; elongated if *b*-/*a*-axes <2/3 and *c*-/*b*-axes ≥2/3; and flat-elongated if *b*-/*a*-axes <2/3 and *c*-/*b*-axes <2/3.

3.4.2. Measuring grains on photos

On photos, we set the lower limit of a measurable grain to 2 mm, based on the pixel resolution of the photos. As outlined in the introduction, the projection of clasts onto the photo plane and the occlusion of clasts by the fine-grained matrix or other clasts (Fig. 1b) could either lead to an underestimation of the grain size and/or to a misidentification of a specific grain axis. We explore both biases by analysing the ratios between the lengths of the *LVA* and *SVA* measured on photos and the grain axes measured with a calliper. Additionally, we tested whether the exposed grain axes on the photos, reflecting the orientation of the grains after deposition, show a dependency on the paleoflow direction.

As mentioned above, images can be distorted, which could introduce a further bias upon data collection. We therefore tested whether the four different photo acquisition methods (*GAD, GAU, RAD, RAU;* see Section 3.3.2) applied to the same outcrops yield identical results (Kolmogorov-Smirnov two-sample (KS2) test, Hodges Jr., 1958). As null-hypothesis H_0 we considered that two grain size distributions are likely identical and drawn from similar populations. The H_0 is tested based on a significance level of alpha = 0.05 corresponding to the 95 % confidence interval.

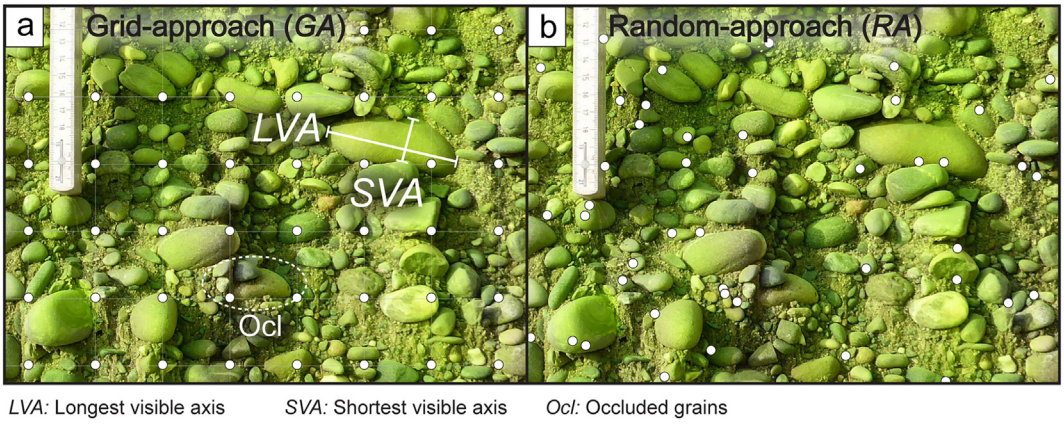

Fig. 3. Two approaches upon measuring grains on photos: a) Coloured outcrop (location 3; Fig. 2) with superimposed grid (Grid-approach, *GA*) or b) with randomly placed dots (Random-approach, *RA*) for grain size measurements on the photos. Please note that the dot size is enlarged for visualisation purposes.

3.4.3. Sieving coarse-grained material

Sieving of the sampled material should significantly reduce or even eliminate a selective bias, as this approach includes the entire range of grain sizes (Leopold, 1970; Attal and Lavé, 2006), and sieving a sufficiently large sample mass can further reduce the errors associated to percentile values. Still, the results can depend on the grain shape particularly if square-hole sieves are used (Fernlund et al., 2007). This is because grains with small *c*-/*b*-axes ratios (flat or flat-elongated grains) are likely to pass to the smaller, lower sieve, whereas grains with large *c*-/*b*-axes ratios (spherical or elongated grains) are retained in the larger sieve (Church et al., 1987; Stähly et al., 2017). To account for this bias, Church et al. (1987) introduced a conversion factor, expressed as the ratio between the sieve mesh size D_s and the length of the *b*-axis of a grain:

$$D_s/b = \frac{1}{\sqrt{2}} * \sqrt{\left[1 + \left(\frac{c}{b}\right)^2\right]} \; [-] \tag{1}$$

Here, *b* and *c* are the grain axes' lengths from the hand data, where the *c*/*b*-ratio denotes the flatness/roundness of a grain (Blott and Pye, 2007). We compared the sieve data (before and after correction) with the outcomes of the other two methods to investigate the effect of this shape correction.

3.5. Percentile and uncertainty calculations

The most used grain size percentiles for hydraulic calculations are the D_{16}, D_{50} or D_{84}. Here, D_i denotes the grain size where *i* percent of all grains are equal to or smaller than this specific length (e.g., Hoey and Ferguson, 1994; Ferguson and Paola, 1997; Green, 2003). The D_{50} is frequently employed for hydraulic calculations because the equivalent grain size is considered to characterize the material particularly during equal mobility conditions in a river (Parker, 1978; Wilcock and McArdell, 1993; Church, 2006). The D_{84} is considered as the frame building grain size of gravel bars (Hey, 1979; Leopold, 1992; MacKenzie and Eaton, 2017; MacKenzie et al., 2018), and the D_{16} acts as counterpart and characterizes the size of the fine-grained fraction (Kondolf and Li, 1992; Leopold, 1992; Bunte and Abt, 2001). For the hand and photo data, the D_{16}, D_{50} and D_{84} grain size percentiles were directly calculated from the grain size datasets. For the sieve data, we translated passed-weight percentages into grain size percentiles by linear interpolation between the sieve bins below and above the target percentiles.

For the calculations of the uncertainties on the hand and photo data, we conducted bootstrapping with replacement where the grain sizes are randomly sampled during 10^4 iterations (see e.g., Rice and Church, 1996 for description). We proceeded similarly to the approach of Mair et al., 2022, but did not consider the modelled measurement errors (see also Eaton et al., 2019, for alternative methods to estimate percentile uncertainties). We calculated the 95 % confidence interval for each of the aforementioned percentiles. We used this confidence interval because not all the hand and photo datasets follow a normal Gaussian distribution. In contrast to the hand and photo data, the sieve data does not contain information on individual grain lengths. Therefore, for each percentile of interest we calculated a lower and upper confidence boundary following Watkins et al. (2020). For instance, error bars on the D_{50} values are expressed by the spread between the D_{45} (lower) and the D_{55} (upper boundary).

Additionally, we calculated how the number of measurements (sample size per site) influences the uncertainties of the percentile values extracted from the hand and photo data. For this, we determined the relative uncertainty on the percentile values (ε_i) following Eaton et al. (2019) where:

$$\varepsilon_i = 0.5 * \left(\frac{CI_{upper} - CI_{lower}}{D_i}\right) * 100 \; [\%] \tag{2}$$

Here, the confidence length (CI_{upper} – CI_{lower}) is dependent on the upper and lower confidence values from bootstrapping based on the 95 % confidence interval. A normalisation by the related percentile values (D_i; e.g., the numerical value of the D_{50}) is required for comparing the uncertainties across the three percentiles of interest and various measuring approaches. A multiplication by 0.5 is applied to account for error margins (i.e., ± uncertainty). We additionally tested whether the uncertainties significantly decrease with a larger number of measurements. We did so by bootstrapping to 400 simulated measurements thereby doubling the sample size.

3.6. Comparison between different datasets

Two different measuring methods yield the same results, if the percentile values, once plotted against each other fit on the 1–1-line, also known as the line of equality, where x = y. This can be tested either visually or statistically. For a statistical test, we used a concordance correlation coefficient (*CCC*) following Lin (1989, 2000), which combines the degree to which all percentiles of a specific method adhere to their linear regression and the correlation between this best-fitting to the 1–1 line. Thus, it quantifies the similarity or discrepancy between the results of two different measurement methods for all percentiles. Here, the *CCC* is computed through:

$$CCC = \frac{2r\sigma_x\sigma_y}{\sigma_x{}^2 + \sigma_y{}^2 + \left(\mu_x - \mu_y\right)^2} \; [-] \tag{3}$$

Here, *r* denotes the Pearson correlation coefficient of the linear regression, σ is the standard deviation, μ is the mean, and σ^2 the variance of the percentile values *x* and *y* derived from two different measuring approaches (e.g., photo and sieve), respectively. Because the *CCC* procedure can only be accomplished on data with ten or more data pairs (Lin, 1989, 2000), we used all percentiles values between the D_{16} and the D_{84} with a spacing of five, starting from the D_{20} and ending with the D_{80} (i.e., D_{16}, D_{20}, D_{25} … D_{80}, D_{84}). For the sake of clarity, the figures encompass the percentiles D_{16}, D_{50}, and D_{84} only. Lin's *CCC* can be considered to indicate a good correlation if the values are >0.80 (Altman, 1990). Thus, if the *CCC* values are close to 1.00, then all percentile values of the two methods are well correlated with respect to the line of equality and to each other (expressed by the Pearson *r*-value; full list in Fig. B.1, Appendix B). We thus used the *CCC* values to identify those measuring methods that yield the highest similarity between the resulting percentile values.

4. Results

4.1. Data consistency

The grain size distributions of all hand datasets indicate that grain sizes <10 mm are scarce, especially for the *a*- and *b*-axes (Hand in Fig. 4). The grain size at site A is generally coarser than at sites B – D, especially for the D_{50} and D_{84} (Fig. 4). This concerns the hand, photo and especially the sieve data. The lengths of the *LVA* and *SVA,* which were measured on the photos of sites A, B and D, display very similar distributions (Fig. 4) that are independent on whether data collection was accomplished on distorted or undistorted photos, and whether grains were randomly selected (*RA*) on the photos or measured if located underneath a grid point (*GA*). This is supported by the results of the KS2 test where almost all comparisons failed to reject the H_0 at varying *p*-values (Fig. B.2, Appendix B), meaning that the individual grain size distributions are comparable to each other. An exception is site C where some of the measurement approaches applied to photos yield in one case a different distribution for the *SVA* values (Fig. 4). In particular, at site C the lengths of the *SVA* appear to be different if the data was collected with either the *GAD* or the *RAU* approach (rejection of H_0 at a very low *p*-value of 0.003 upon

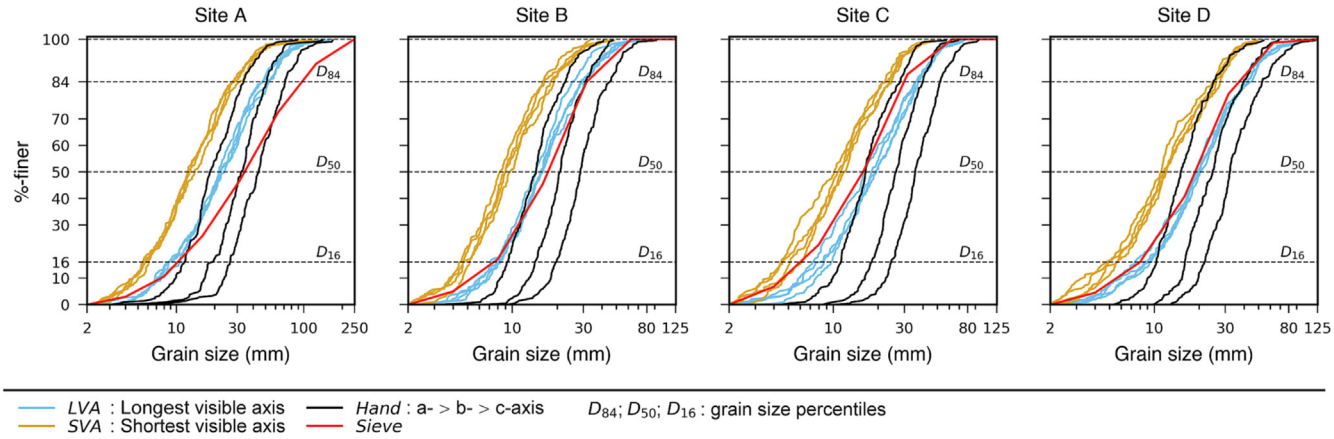

Fig. 4. Grain size distributions: Data expressed as %-finer for all acquisition methods per sample sites A, B, C and D. Please note the logarithmic scale. The positions of the grain size percentile values (D_{16}, D_{50}, D_{84}) are marked by horizontal lines.

comparing the two datasets; Fig. B.2, Appendix B). Further details are shown in figures and Tables A.1 – A.4 (both Appendix A) for the curves of the grain size distributions and for the percentile values with confidence intervals and relative uncertainties, respectively.

4.2. Comparison of percentile values

4.2.1. Photo versus sieve data

The closest similarity between the data can be found when comparing the *LVA* data collected on photos with the sieve data (*LVA* in Fig. 5a). This is particularly the case for datasets (and all related percentiles) collected with the *GAD, GAU, RAD* and *RAU* approaches at sites B – D, and this is also illustrated by the corresponding *CCC* (Eq. (3)) values >0.9 (Fig. 5a). At site A, the *LVA* photo values deviate from such a correlation with the sieve data (average *CCC* value of 0.53; Fig. 5a), particularly for the D_{50} and D_{84}. In contrast, at all sites, the D_{50} and D_{84} values of the *SVA* (measured on photos) tend to be lower than the corresponding percentile values of the sieve data. The finer grained fraction (D_{16}) of both methods, photo measurements and sieving, yielded relatively consistent results (*SVA* in Fig. 5a). Yet the corresponding average *CCC* values are all below <0.70 and thus below the threshold of 0.80 (*SVA* in Fig. 5a). A complete table of all individual *CCC* values is shown in Fig. B.3 (Appendix B).

4.2.2. Photo versus hand data

The lengths of the *LVAs* measured on photos are consistently shorter than those of the hand *a*-axes (*a*-axis in Fig. 5b). In contrast, measurements of the *LVA* yield D_{84} values that are comparable to the related percentile values of the hand *b*-axes. Regarding the D_{16} and D_{50}, however, the correlations between the related hand and photo values are only moderate (*b*-axis in Fig. 5b). Despite that, only site D has an average *CCC* value >0.87 if the comparison of the *LVA* with the hand *b*-axis and all percentile values are considered. A comparison of the *LVA* with the hand *c*-axes shows that the D_{84} percentile values of the photo data are larger than those of the hand data in most of the cases, whereas the D_{16} and D_{50} are in relatively good agreement (*c*-axis in Fig. 5b). Average *CCC* values for all percentiles are only above the threshold of 0.80 for site B, whereas they are below it for sites A, C and D in case of the hand *c*-axes (Fig. 5b). Measurements of the *SVA* on the photos yield percentile values that are generally smaller than those of the hand *a*-, *b*- and *c*-axes in almost all cases (Fig. 5c). In particular, only the D_{84} value of the hand *c*-axis is comparable to the corresponding percentile values of the *SVA* photo data, especially for site D (average *CCC* value of 0.81 for all percentiles; Fig. 5c).

4.2.3. Hand data versus sieve data

All percentile values of the hand *a*-axis data are clearly larger than those of the sieve datasets at sites B – D, yet site A shows an acceptable correlation between them (*CCC* = 0.80). Although the measurements of the hand *a*-axes of site A revealed larger D_{16} and smaller D_{84} values than sieving the same material, both methods return comparable D_{50} values (*a*-axis of site A, Fig. 5d). The hand *b*-axis data show good correlations to the sieve datasets only for the D_{84} (sites B and D), and moderate correlations for the D_{50} (sites A, B and D), respectively. In contrast, all D_{16} values of the hand *b*-axes are generally larger than the corresponding percentile values resulting from sieving (*b*-axis in Fig. 5d). Overall, sites B and D are best correlated if the lengths of the hand-*b*-axes and sieve-axes and all percentiles are considered (both *CCC* = 0.83 in average). The hand *c*-axes show a good correlation to the sieve data for the D_{16} (sites A, B and D), whereas site C shows a better correlation for the D_{50}. The data at site C has the highest average *CCC* = 0.89 for all percentiles (*c*-axis in Fig. 5d).

4.3. Uncertainty estimates

For all hand datasets and for 200 measurements, the relative uncertainties (ε_i; Eq. (2)) are on average ± 7.82 % for the D_{16}, ±6.97 % for the D_{50} and ± 9.87 % for the D_{84} (Table 3). For 400 measurements, the relative uncertainties for the hand data are reduced to ±5.71 % for the D_{16}, ±4.83 % for the D_{50}, and to ±6.60 % for the D_{84} on average (Table 3). These relative uncertainties (95 % confidence interval) concern all three grain axes measured by hand and calliper.

For the photo data (both *LVA* and *SVA*; see Table 3 for details) and for all photo acquisition methods, the average relative uncertainties are c. ±17.45 % for the D_{16}, ±12.99 % for the D_{50} and ± 14.30 % for the D_{84}. For 400 measurements, the average relative uncertainties for the photo data decrease to ±13.81 % for the D_{16}, ±9.37 % for the D_{50}, and to ±9.87 % for the D_{84} (Table 3). These uncertainties (95 % confidence interval) are independent of the grain axes (*LVA* and *SVA*). They concern all grain size percentiles (D_{16}, D_{50}, D_{84}), all sites A – D, and all approaches through which the photos were processed (distorted versus rectified photos) and the grains were selected on these photos (grains selected on a grid versus random selection of grains).

The average uncertainties of the sieve data (expressed by a lower and upper boundary of ±5 percentiles) are ±21.37 % for the D_{16}, ±12.13 % for the D_{50}, and ± 17.55 % for the D_{84} (Table 3). All individual uncertainty values are shown in Tables A.1–A.4 (Appendix A). Fig. B.7 (Appendix B) shows the relative uncertainties of the hand and photo data plotted against increasing sample size.

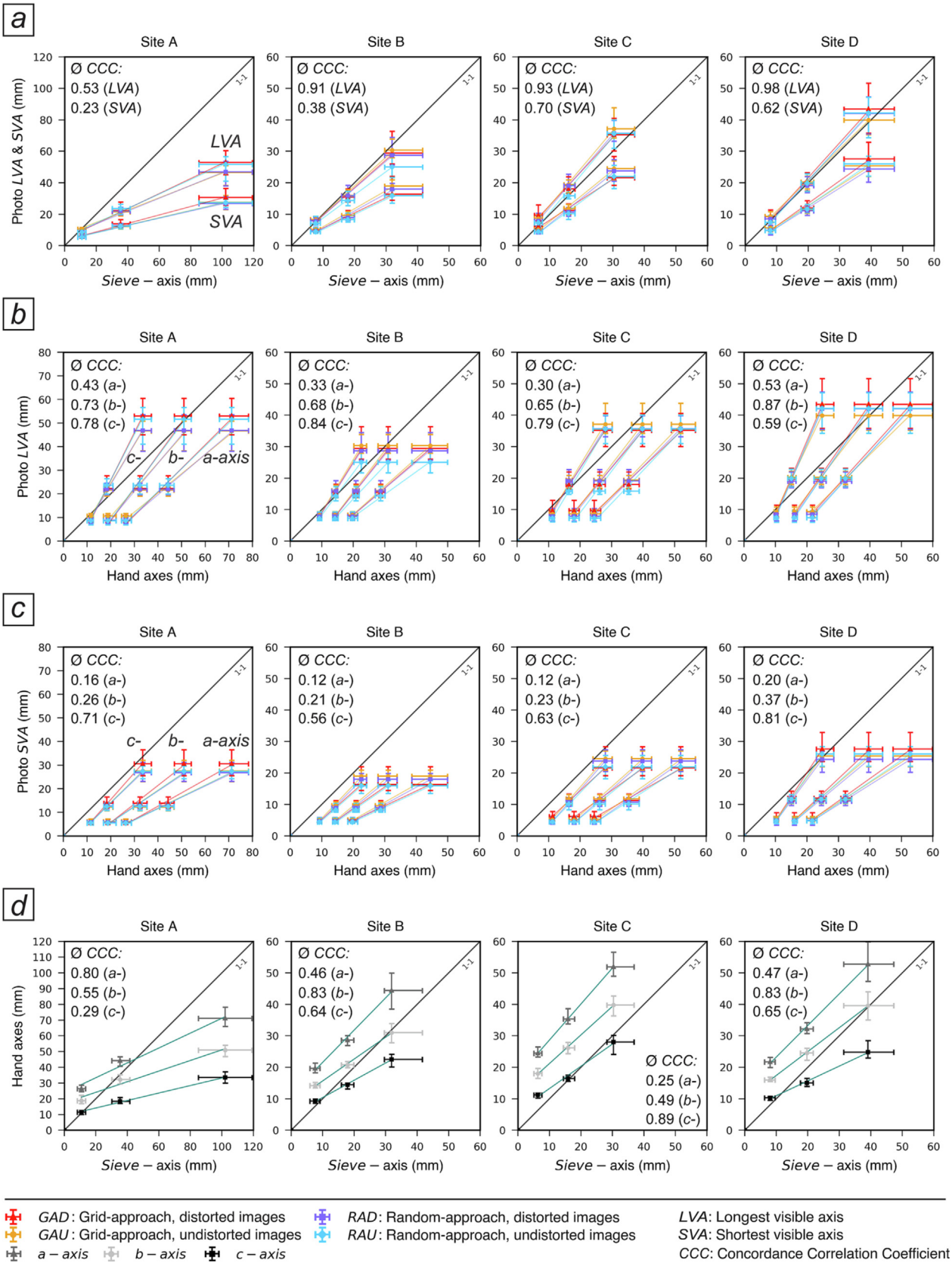

Fig. 5. Comparison of percentile values from different measuring approaches: a) Comparison between the photo and the sieve data. b) Comparison of the hand data with the longest visible axis (*LVA*) and c) the shortest visible axis (*SVA*) on photos. d) Comparison between the hand and the sieve data. Percentile values in increasing order (i.e., $D_{16} < D_{50} < D_{84}$). Error bars represent the 95 % confidence interval (hand and photo data). The sieve data uncertainties show a confidence range of ±5 percentiles. Numbers represent average *CCC* values.

Table 3
Uncertainties on the percentiles: Relative uncertainties are based on the 95 % confidence interval (hand and photo data) or on a confidence range of ±5 percentiles (sieve data).

Average relative uncertainty ε for all sites [± %]	ε_{16} (n = 200)[a]	ε_{16} (n = 400)[a]	ε_{50} (n = 200)[a]	ε_{50} (n = 400)[a]	ε_{84} (n = 200)[a]	ε_{84} (n = 400)[a]
Hand data (*a*-, *b*-, *c*-axes)	7.82	5.71	6.97	4.83	9.87	6.60
Photo data (*LVA*)	18.46	13.81	13.14	9.37	13.91	9.87
Photo data (*SVA*)	16.49	13.81	12.83	9.36	14.69	9.86
Sieve data (*Ds*)	21.37	–	12.13	–	17.55	–

Ds: Sieve-axis (Sieve-mesh size); ***LVA***: Longest; and ***SVA***: shortest visible axis (incl. All measuring approaches on photos).
[a] Sample size is valid for hand and photo data only. See Table 1 for sieve sample mass.

4.4. Influence of grain shape and paleoflow direction

The ratios between the individual axes remain stable, over the entire range of grain lithologies and are independent of the grain size and the sample sites. On average, the *b*/*a*-axes ratio is c. 0.74, whereas the c/*b*-axes ratio is c. 0.67 (Table 4). Also, for all sites, the shape classification reveals that the majority of the grains are either flat (in average c. 38 %) or spherical (c. 34 %), whereas the rest corresponds to elongated (c. 17 %) or flat-elongated grains (c. 11 %; Table 5). Additionally, grain shapes are not correlated to the lengths of the hand *b*-axis nor to the *a*- and *c*-axis, in the sense that the shape classes spread over various grain sizes. Further details on the grain shape in relation to the *a*-, *b*- and *c*-axes of the hand data are shown in Fig. A.5a, b and c (Appendix A), respectively.

The influence of the grains' shape on the sieving results is evaluated using Eq. (1). The average D_s/*b*-ratio of c. 0.85 (Table 4) for all four sites shows that the percentile values of the sieve data are c. 15 % smaller than the corresponding values of the hand *b*-axes. Applying this factor to the sieve data thus yields in c. 15 % larger percentile values compared to those before the correction (e.g., Fig. 5a and d). The comparison of these corrected values (sieve data) with the results of the other grain size measuring methods shows that such corrections do not significantly improve the *CCC* values and thus the correlations (Fig. B.4, Appendix B).

The comparisons of the grain size percentiles in relation to the exposure of the outcrop relative to the paleoflow (Fig. 2a) reveal that both, the *LVA* and *SVA* percentile values of site A, are generally larger than those of the perpendicularly oriented site B. This is particularly the case for the D_{50} and D_{84} values (Fig. 6). In contrast, the *LVA* and *SVA* of sites C and D (which are perpendicular to each other) disclose very similar percentile values, only the D_{84} values of site D are slightly larger than those of site C (Fig. 6).

4.5. Corrections of photo data to account for occlusion effects

Our results reveal that the lengths of the *LVAs* lay in general somewhere between those of the hand *b*- and *c*-axes (i.e., *a*-hand-measured > *b*-hand-measured ≥ *LVA* ≥ *c*-hand-measured; Fig. 5b), if considering the percentiles of interest. The lengths of the *SVA* measured on photos slightly underestimate, but generally correspond to those of the hand *c*-axis (Fig. 5c). By comparing the lengths of the *LVAs* (of all measuring approaches on images) to the hand *b*-axes, we found an average ratio of 0.83 for all sites (*LVA*/*b* in Table 4). In the same sense, the average ratio of the lengths of all *SVAs* and the lengths of the hand *c*-axes is 0.76 (*SVA*/*c* in Table 4). We corrected the *LVA* and *SVA* datasets by these factors and compared these new values with the hand *b*-axis datasets. Consequently, the values for data derived through both methods only slightly better aligned to each other for the D_{16}, whereas the same corrections resulted in a better correlation of the D_{50} (Fig. 7). Yet the alignment between the D_{84} values becomes worse but remains acceptable (Fig. 7). Besides, we found that for all percentiles the correlations between the photo and hand data highly improve (*CCC* values >0.80; Fig. 7 and Fig. B.5, Appendix B). Corrections by other ratios (i.e., *LVA*/hand-*a*; *LVA*/hand-*c*; *SVA*/hand-*a;* and *SVA*/hand-*b*; Table 4) do not improve the correlations of the percentile values between the photo and hand data.

Table 4
Grain axes' ratios: Based on the hand data (numbers rounded to 2 decimals).

Axes ratios [−]	Site A	Site B	Site C	Site D	Average
b/*a*	0.74	0.73	0.74	0.75	0.74
c/*b*	0.64	0.70	0.66	0.66	0.67
Ds/*b*	0.85	0.87	0.85	0.85	0.85
LVA/*a*	0.60	0.58	0.57	0.66	0.60
LVA/*b*	0.82	0.81	0.78	0.90	0.83
LVA/*c*	1.30	1.18	1.19	1.40	1.27
SVA/*a*	0.35	0.35	0.34	0.39	0.36
SVA/*b*	0.49	0.50	0.47	0.53	0.50
SVA/*c*	0.78	0.71	0.72	0.83	0.76

a, ***b***, ***c***: Grain axes (hand data); ***Ds:*** Sieve-axis (Sieve-mesh size); ***LVA***: Longest; and ***SVA***: shortest visible axis (incl. All measuring approaches on photos). Averages calculated from unrounded values per site.

5. Discussion

5.1. Biases related to data collection and measuring approaches

As shown by the results, the material at site A is coarser grained than at the other sites B – D and contains grains that are larger than 125 mm (largest sieve-mesh size; Figs. 4 and 5). This allows us to explore, for site A, how the occurrence of such large grains adds a bias to the calculations of the percentile values. In particular, the hand data of site A comprises the lengths of 3 grains and the photo data of 1–2 grains (depending on the photo acquisition method) that were larger than the threshold of 125 mm. Removing these grains from the datasets do not significantly lower the percentile values of the D_{16}, D_{50} and D_{84} of both the hand and photo data. However, the sieve data of site A contains 4 grains >125 mm, which are 4.6 kg and contribute c. 9.3 % to the sample mass after fines <2 mm were removed (or c. 7.6 % to the bulk-mass). Upon removing these 4 grains from the sieve dataset, the D_{50} and especially the D_{84} are shifted towards smaller size values, and the corresponding *CCC* values for sample site A are consequently higher. This is illustrated for the comparison between the photo with the sieve data, where the average *CCC* values (site A in Fig. B.6, Appendix B) for all percentiles shifted from 0.53 to now 0.97 (*LVA*) and from 0.23 to 0.64 (*SVA*). Although the sieve data were within acceptable uncertainty ranges concerning the sample weight, they are sensitive to a few large and heavy grains and thus sensitive to the particle shapes and the way of how clasts pass through the sieve openings (Church et al., 1987; Fernlund et al., 2007; Attal et al., 2015).

Data collection by hand is prone to under-sampling of grains <10 mm (Fig. 4). Furthermore, considering all percentile values, the lengths of the hand-axes reveal the least consistent correlation to those of

Table 5
Grain shapes: Classification after Zingg (1935) based on the grain axes ratios (hand data; rounded numbers, 1 % rounding error).

Grain shape classes [%]	Site A	Site B	Site C	Site D	Average
Flat ($b/a \geq 2/3$ & $c/b < 2/3$)	43.0	31.0	37.0	40.0	38.0
Spherical ($b/a \geq 2/3$ & $c/b \geq 2/3$)	29.0	39.0	34.0	33.0	34.0
Elongated ($b/a < 2/3$ & $c/b \geq 2/3$)	16.0	21.0	16.0	16.0	17.0
Flat-elongated ($b/a < 2/3$ & $c/b < 2/3$)	13.0	9.0	12.0	10.0	11.0

a, ***b***, ***c***: Grain axes (hand data).

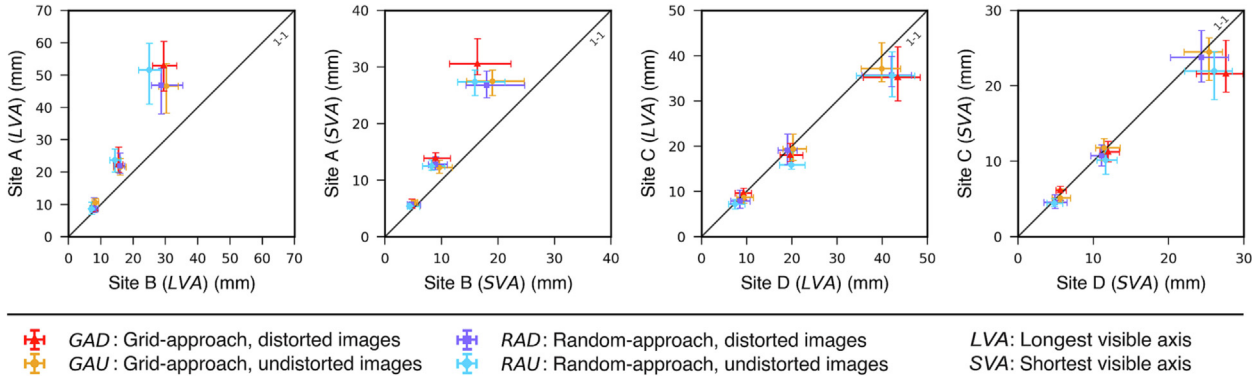

Fig. 6. Photo data in relation to paleoflow direction: Comparison of percentile values (in increasing order, i.e., $D_{16} < D_{50} < D_{84}$) of sites with different orientations with respect to the paleoflow (see Fig. 2a for orientation of sites).

resulting from the other measuring approaches, which is supported by large variations of the *CCC* values (Fig. 5b and c). Even though the sampling was effectuated blindly, under-sampling of smaller grains is likely because larger grains tend to be unintentionally favoured upon picking (e.g., Marcus et al., 1995; Wohl et al., 1996; Daniels and McCusker, 2010). The under-sampling thus results in narrower underlying grain size distributions of the hand data, which likely yield in low uncertainties (Eaton et al., 2019; Table 3). The inconsistent correlations between the hand data and those collected with the other two methods might also reflect the lower precision upon measuring large, small, or irregular-shaped grains that are difficult to handle (Fripp and Diplas, 1993; Marcus et al., 1995). Yet our approach bears the advantage that the operator measured all available axes and had not to determine the length of a specific axis only (e.g., the *b*-axis), which sometimes has not been done in previous studies.

Grain size measurements on photos yield precise, consistent, and unbiased datasets, if performed by the mentioned sampling procedures. The result of the KS2 test shows that the various acquisition methods (*GA* and *RA*) and photo-specific factors (distorted and undistorted photos) yield comparable grain size datasets (Fig. B.2, Appendix B). The average relative uncertainties (95 % confidence interval and thus considering two standard deviations of the mean) on the grain size percentile values of

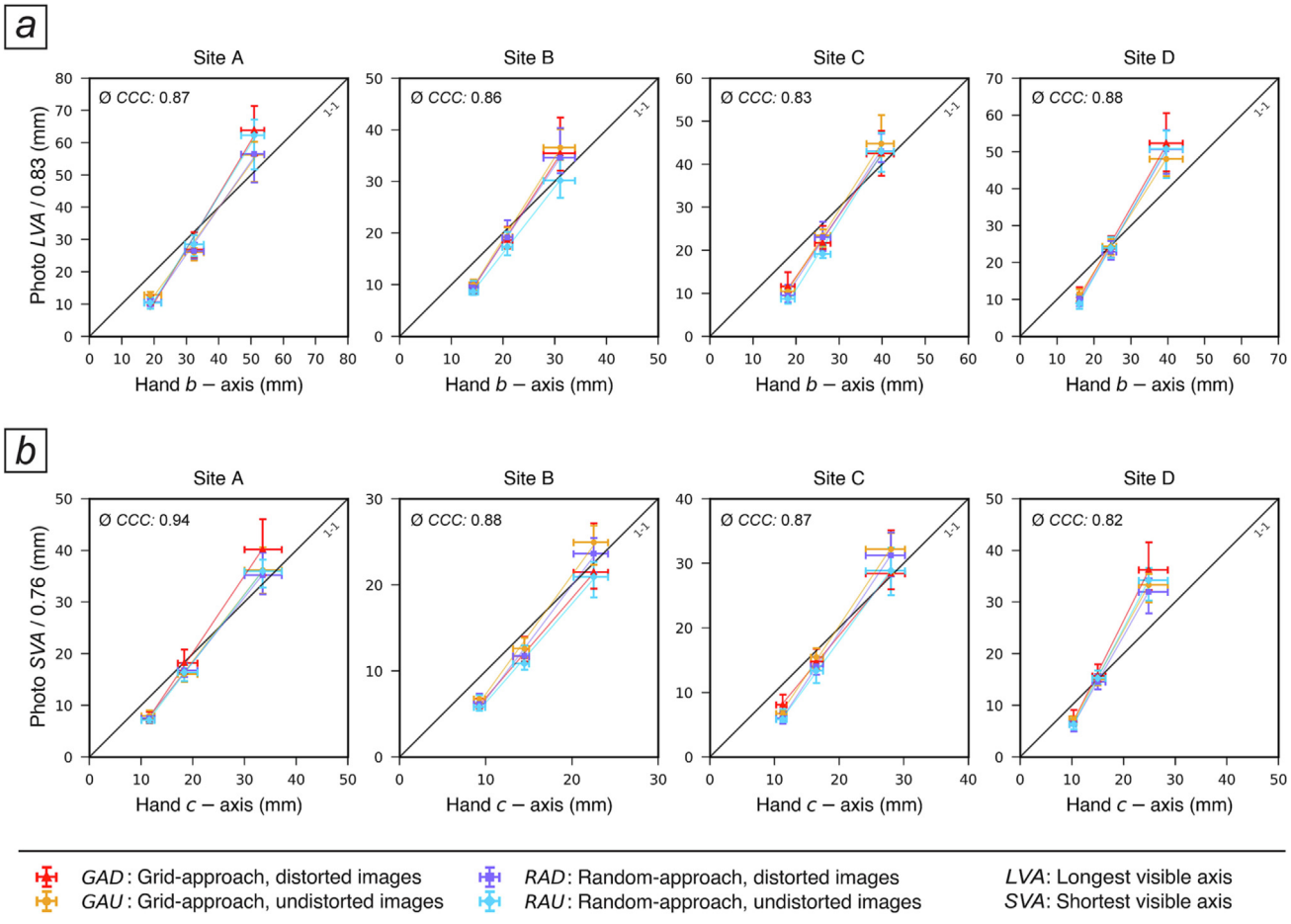

Fig. 7. Comparison of percentile values of the corrected photo data: The photo data is now corrected by a) the average *LVA*/hand *b*-axes ratios of 0.83, and b) the average *SVA*/hand *c*-axes ratios of 0.76. Percentile values in increasing order (i.e., $D_{16} < D_{50} < D_{84}$). Error bars represent the 95 % confidence interval. Numbers represent average *CCC* values (Concordance correlation coefficient).

the photo data (both *LVA* and *SVA*) range between ±12.83–18.46 % for 200 grains (Table 3 and Fig. B.7, Appendix B). Such values were considered as acceptable for coarse-grained material (e.g., Whittaker et al., 2011; Guerit et al., 2018; Eaton et al., 2019; Watkins et al., 2020).

5.2. Influence of particle shape, outcrop orientation and grain occlusion

The ratios between the individual hand axes (Table 4), and thus the general grain shape (Table 5), are identical at all sites, and they are in concordance with the outcomes of previous studies that present similar axes' ratios for coarse-grained fluvial deposits (e.g., Paola and Mohrig, 1996; Litty and Schlunegger, 2017). The grain shapes are furthermore independent of the lengths of the *b*-axes. Moreover, the axes' ratios of the coarse-grained material used in this study are similar to those reported for Alpine conglomerate beds (Tanner, 1944; Haldemann, 1948; Bürgisser, 1980), most likely because parts of the material in the gravel pit was derived from these (Pfander et al., 2022).

We further investigated the influence of the grain flatness/roundness on the outcomes of sieving the material. By applying a correction of c. +15 % to the percentile values of the sieve data (that is based on the average D_s/b-ratio of 0.85; Table 4), we particularly expected an improvement of the relationships between the sieve-axes and the hand *b*-axes' percentile values, which was generally not the case (Fig. B.4, Appendix B). Yet, our calculated D_s/b-ratios reflect the outcome of other studies (Graham et al., 2010; Stähly et al., 2017), notably calculated for flat-lying grains only, showing that grain size lengths of the sieve data indeed underestimate the lengths of the hand *b*-axes. Note that this observation also considers possible biases upon measuring grains by hand and calliper. Nevertheless, we anticipate that the measuring approach with callipers provide the least biased datasets, and because it is the only method that provides information on all three grain axes, we use this data as benchmark for further discussion. Accordingly, we propose that the ratio between the lengths of the *LVA* and the hand *b*-axes can be used to correct for effects that result from the occlusion of grains and from distortions through projections on photos. Applying the *LVA*/hand-*b* and *SVA*/hand-*c* ratios (Table 4) to correct for these effects improves the comparison between the hand and photo percentile values for the D_{16} and especially for the D_{50} (Fig. 7). For the D_{84}, such a correction only slightly worsens the correlation between the hand and photo data, but the related uncertainties are acceptable (Fig. 7). Because *CCC* values consider all these percentiles, recalculations thereof revealed a highly better correlation between the hand data and the corrected photo datasets (Fig. B.5, Appendix B). Therefore, we consider that these ratios, considering the entire grain size distribution, reflect the degree to which the lengths of the grain axes are underestimated on photos from outcrops, which is c. 17 % (i.e., 0.83) for the *LVA* and c. 24 % (i.e., 0.76) for the *SVA* (both Table 4). These values agree with similar outcomes from previous studies (Storz-Peretz and Laronne, 2013). Moreover, the average *LVA*/hand-*b* ratio of c. 0.83 is very consistent with the average D_s/b ratio of c. 0.85 (Table 4). This explains the significantly good correlations between grain size data collected through sieving and measurements on photos, because both methods yield lower *b*-axis values than measuring the material by hand and calliper. Similar effects have been observed for datasets collected on outcrops (Storz-Peretz and Laronne, 2013) and for flat-lying deposits (Adams, 1979; Stähly et al., 2017).

The dependency of the sample site orientations related to the paleoflow direction revealed no clear influence on the lengths of the exposed grain size axes measured on photos (*LVA* and *SVA;* Fig. 6). Particularly the outcrops of sites C and D, which are oriented perpendicular to each other, revealed similar *LVA* and *SVA* datasets. We therefore infer that the lengths of the exposed grain axes are independent on the outcrop orientation. We acknowledge that the data of site A depart from this picture, probably because the material is generally coarser grained than at the other sites.

6. Conclusions

Grain size measurements from outcrops with orientations (sub-) vertical to the initial bedding can be best achieved by photo-analysis. Our study reveals that the applied measuring approaches where grains are either randomly selected on a photo (random-approach; *RA*) or depicted if they occur on a grid intersection (grid-approach; *GA*) yield directly comparable and statistically similar grain size datasets. Our data additionally shows that photo-specific factors (distorted and undistorted photos) seem not to play a crucial role in short-distance surveys (c. 1–1.5 m from outcrops) with hand-held cameras. Also, the orientation of the outcrops relative to the paleoflow direction does not have a measurable impact on the grain size datasets. Uncertainties considering the 95 % confidence interval of the percentile values for all datasets where 200 grains were measured on photos are on average ±16.45 % for the D_{16}, ±12.80 % for the D_{50} and ±14.00 % for the D_{84}.

Measurements of the longest visible axis (*LVA*) on photos yield datasets that show a good correlation with grain size data established through sieving the same material. Both methods, however, underestimate the length of grains measured by hand with a calliper. If the lengths of these hand *b*-axes are taken as a reference, the sieving of the material underestimates these lengths by c. 15 %, whereas measurements on photos (*LVA*) yield in an underestimation of c. 17 %. The same is also the case where the lengths of the shortest visible axes (*SVA*) are measured on photos, which yields in an underestimation of the hand-measured *c*-axes by c. 24 %. These underestimations are either based on the particles' shape expressed by the ratio between the size of the sieve mesh size (*Ds)* and the lengths of the hand-measured *b*-axes or explained by the occlusion of grains and their projection onto photos.

Finally, we find that the *LVA* measured on photos are comparable to the corresponding datasets where the *b*-axes were measured by hand with callipers, after some corrections are made. Such a correction is considering possible effects of grain occlusion and a foreshortened projection of grains onto the photo plane. Accordingly, we suggest correcting the underlying grain size distributions by c. +17 %, yielding in significant good correlations between the hand and photo data for the D_{50} and the D_{16}. Interestingly, good agreements remained for the D_{84} of both datasets after such corrections (Fig. 7a).

We close our work with the following recommendations for measuring grains >2 mm on outcrops of fluvial gravel and conglomerate:

1) Take photos at a distance of 1–1.5 m and as perpendicular as possible to the outcrop.
2) Ignore the outer c. 10 cm from the photo frame as they have the largest distortion. Photo corrections through photogrammetric methods are not necessary for such short distance surveys.
3) Either use a regularly spaced grid on the photos or randomly placed dots to mark the grains to be measured, and then measure the grains under multiple dots only once.
4) Measure the longest visible axis of at least 200 grains on one or more images from the same site.
5) Correct the underlying grain size distribution and thus the percentiles D_{16}, D_{50} and D_{84} by +17 %.

CRediT authorship contribution statement

The study has been created by PG with help by FS, AHP and DM. PG, AHP, DM collected the samples, PG analysed the data and interpreted the results with help by AHP, DM, GAD, FN and FS. PG wrote the text with help by FS, AHP, DM, GAD and FN. All authors contributed to the interpretation of the results and the discussion of the study.

Funding sources

This work was supported by the Swiss National Science Foundation (SNSF) [P1BEP2_200189].

Data availability

The raw data and the digital photos are available in the electronic appendix.

All calculations were implemented in Python 3. The repository of the Python files is available on GitHub: https://github.com/garefalakis/Gravel-Pit.git

Declaration of competing interest

The authors declare the following financial interests/personal relationships which may be considered as potential competing interests: Philippos Garefalakis reports financial support was provided by the Swiss National Science Foundation.

Acknowledgments

We thank N. Akçar and J. Pfander for the photos (Figs. 1c and 2b) of the gravel pit and thank J. Pfander for help to get access to the gravel pit and help with collection of the material. We thank the Berner Fachhochschule (BFH) for providing access to their laboratory sieving facilities.

The authors would like to thank Professor Brian Jones for handling our paper and thank the helpful reviews by Professor Carita Augustsson and Professor John S. Armstrong-Altrin, which helped to clarify and strengthen the arguments made in this paper.

Appendix A

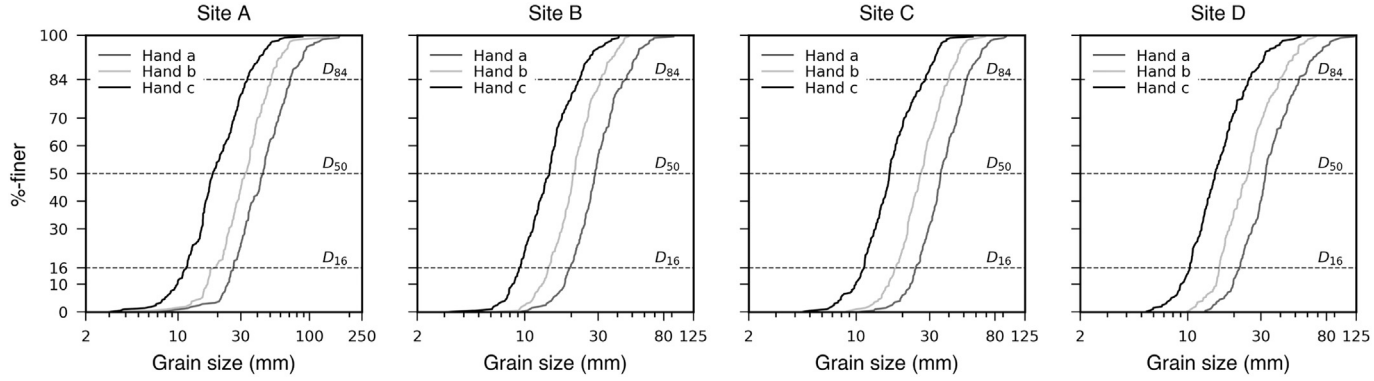

Fig. A.1. Hand data: Grain size distribution for the *a*-, *b*- and *c*-axis from the hand data per sample site. The positions of the grain size percentile values (D_{16}, D_{50}, D_{84}) are marked by horizontal lines.

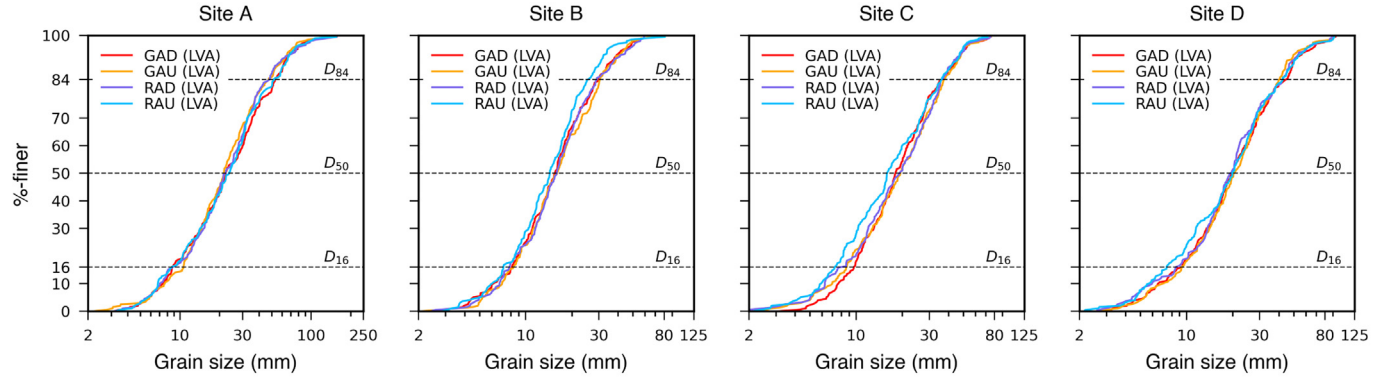

Fig. A.2. Photo data (*LVA*): Lengths of the longest visible axis (*LVA*) of all sample sites from photo data. ***GAD***: Grid-approach, distorted photos; ***GAU***: Grid-approach, undistorted photos; ***RAD***: Random-approach, distorted photos; ***RAU***: Random-approach, undistorted photos. The positions of the grain size percentile values (D_{16}, D_{50}, D_{84}) are marked by horizontal lines.

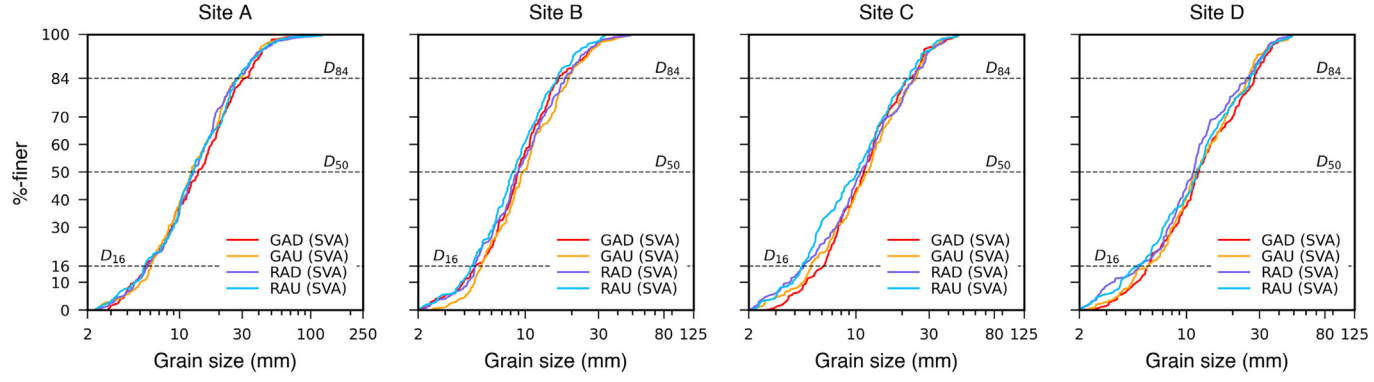

Fig. A.3. Photo data (*SVA*): Lengths of the shortest visible axis (*SVA*) of all sample sites from photo data. ***GAD***: Grid-approach, distorted photos; ***GAU***: Grid-approach, undistorted photos; ***RAD***: Random-approach, distorted photos; ***RAU***: Random-approach, undistorted photos. The positions of the grain size percentile values (D_{16}, D_{50}, D_{84}) are marked by horizontal lines.

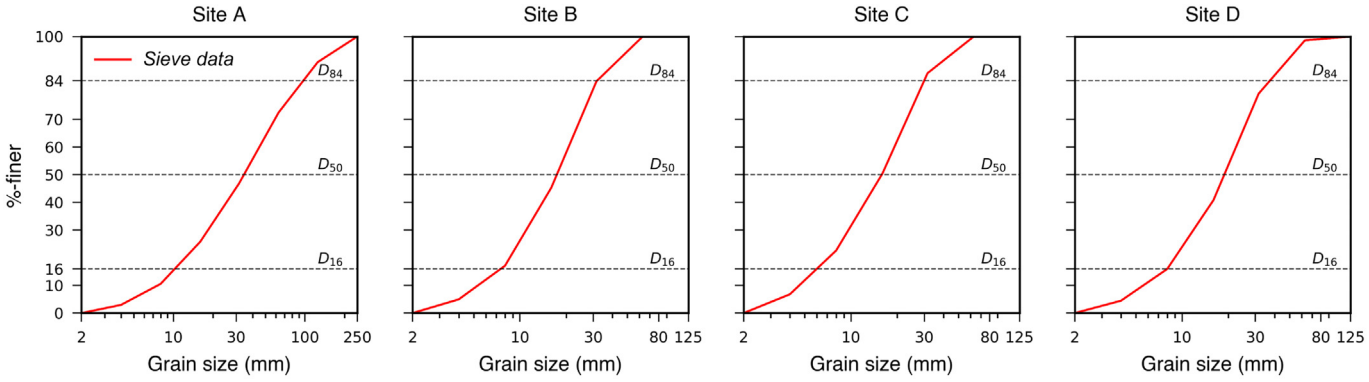

Fig. A.4. Sieve data: Distribution of the sieve data of all sample sites. The positions of the grain size percentile values (D_{16}, D_{50}, D_{84}) are marked by horizontal lines.

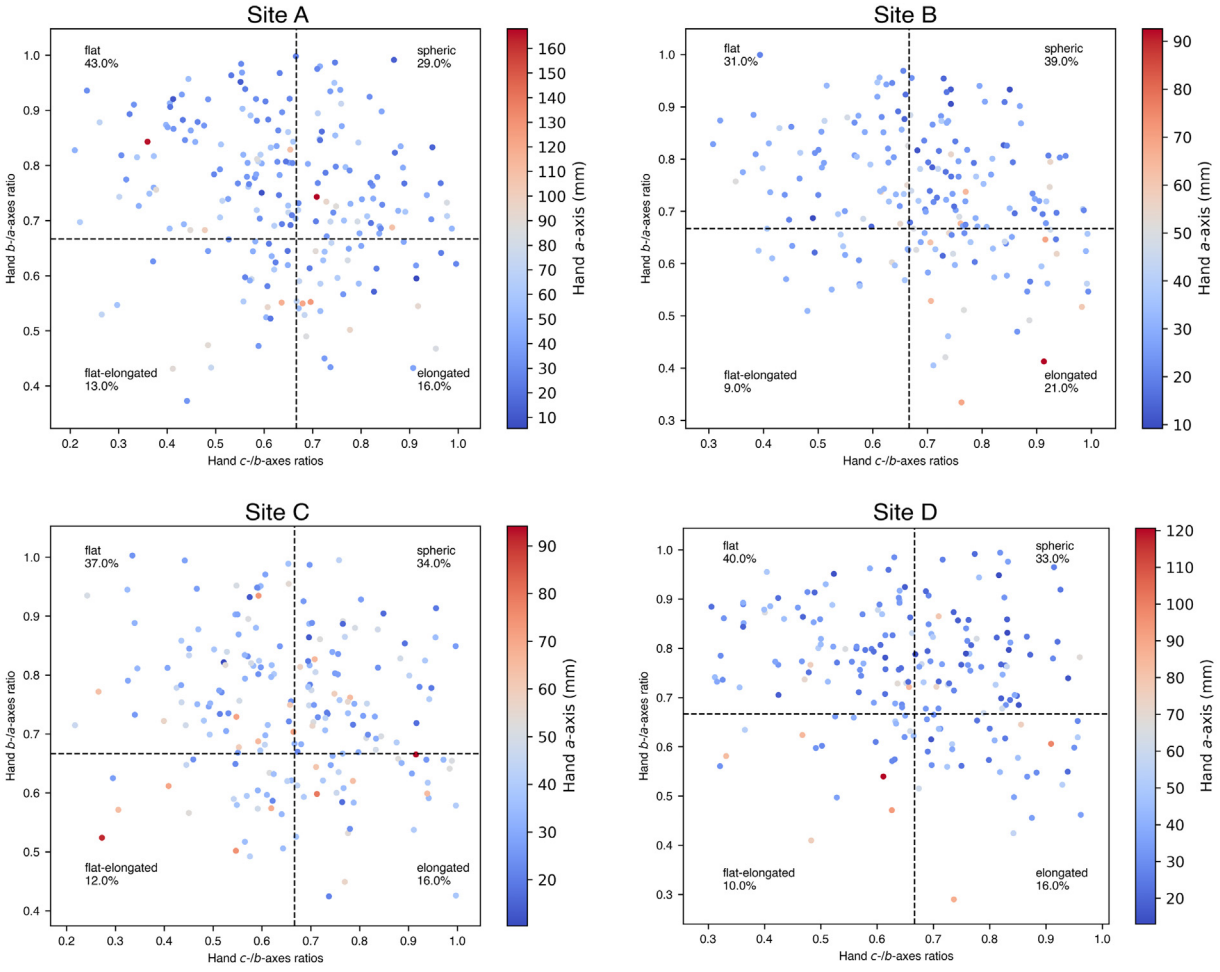

Fig. A.5. Grain shape classification: Grain shapes expressed by the hand *b*-/*a*- and hand *c*-/*b*-axes ratios versus grain sizes of the a) hand *a*-axis; b) hand *b*-axis, and c) hand *c*-axis, respectively. Numbers of grain shape classes are rounded (1% rounding error).

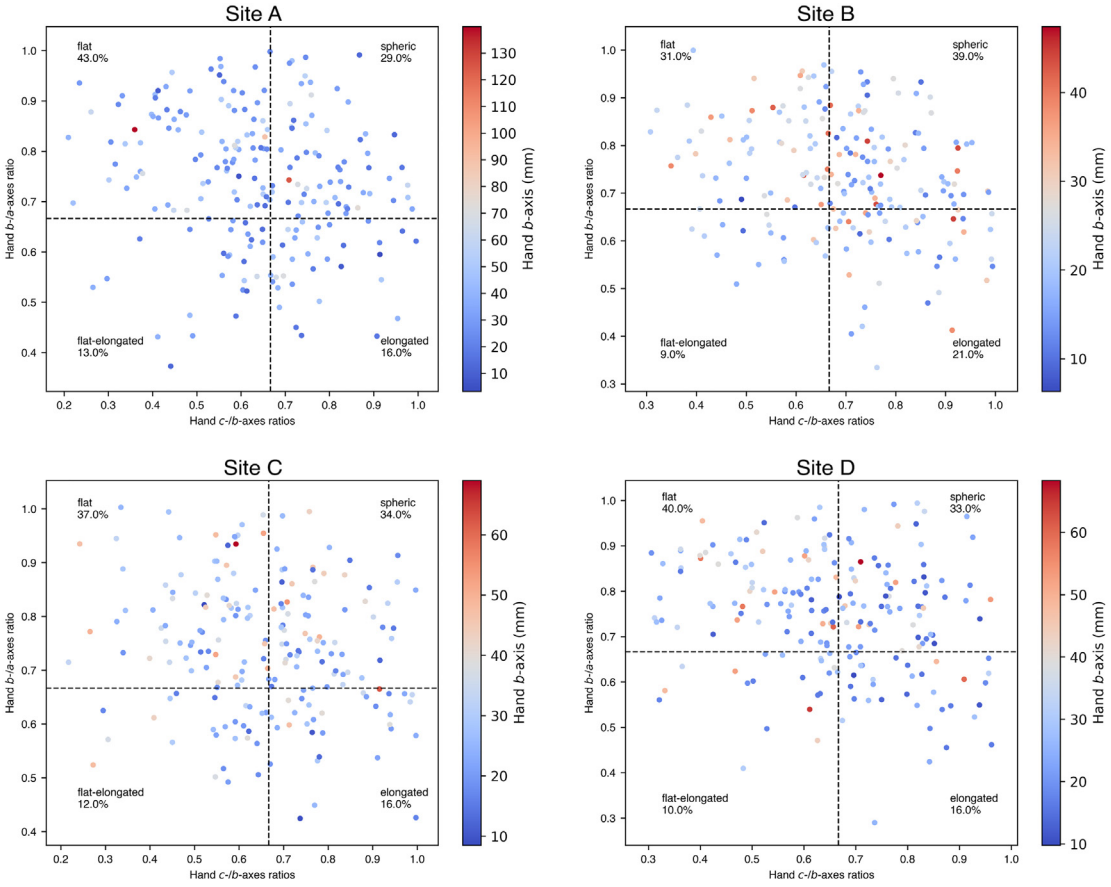

Fig. A.5 (*continued*).

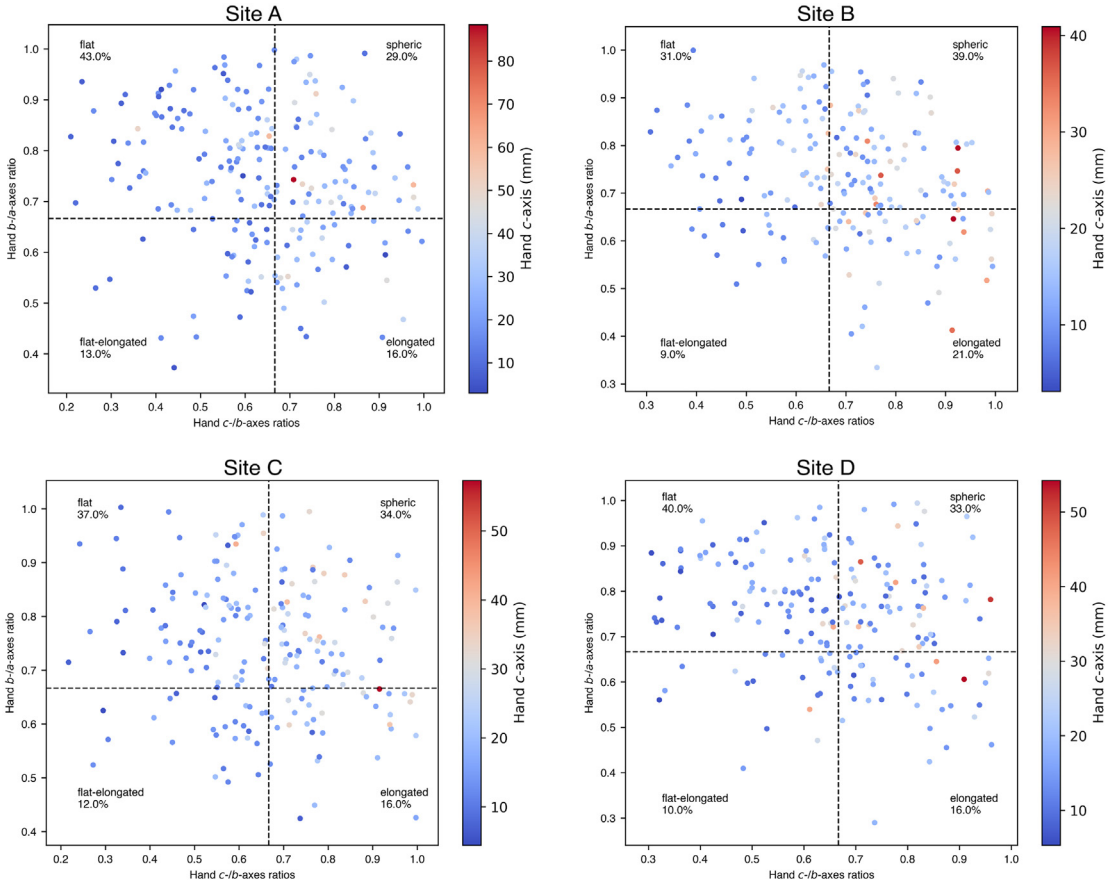

Fig. A.5 (*continued*).

Table A.1
a)–c) Percentile values and relative uncertainties of the hand data: Percentile values (D_{16}, D_{50}, D_{84}) and 95% confidence interval (CI) of all sample sites from hand data.

A.1a

Hand *a*-axis	D_{16} [mm]	95% CI [mm]	ε_{16} [±%]	D_{50} [mm]	95% CI [mm]	ε_{50} [±%]	D_{84} [mm]	95% CI [mm]	ε_{84} [±%]
Site A	26.37	[24.58 – 28.70]	7.81	44.28	[40.71 – 46.71]	6.78	71.16	[66.03 – 78.28]	8.61
Site B	19.69	[18.28 – 21.34]	7.77	28.67	[26.96 – 30.03]	5.35	44.41	[38.55 – 49.92]	12.80
Site C	24.47	[23.32 – 26.49]	6.48	35.40	[33.81 – 38.69]	6.89	51.92	[48.95 – 56.56]	7.33
Site D	21.75	[19.91 – 23.18]	7.51	32.19	[30.74 – 34.17]	5.33	52.79	[47.29 – 59.87]	11.91

A.1b

Hand *b*-axis	D_{16} [mm]	95% CI [mm]	ε_{16} [±%]	D_{50} [mm]	95% CI [mm]	ε_{50} [±%]	D_{84} [mm]	95% CI [mm]	ε_{84} [±%]
Site A	18.82	[16.92 – 22.20]	14.03	32.28	[29.52 – 35.31]	8.97	50.98	[46.90 – 54.08]	7.04
Site B	14.20	[13.47 – 15.17]	5.99	20.82	[19.84 – 21.83]	4.77	31.02	[27.82 – 33.89]	9.79
Site C	18.05	[16.50 – 19.69]	8.83	26.22	[24.35 – 27.94]	6.85	39.80	[36.37 – 42.70]	7.95
Site D	16.01	[15.54 – 16.91]	4.29	24.58	[22.26 – 26.06]	7.73	39.57	[35.07 – 44.00]	11.28

A.1c

Hand *c*-axis	D_{16} [mm]	95% CI [mm]	ε_{16} [±%]	D_{50} [mm]	95% CI [mm]	ε_{50} [±%]	D_{84} [mm]	95% CI [mm]	ε_{84} [±%]
Site A	11.56	[10.03 – 12.55]	10.92	18.34	[17.08 – 20.88]	10.36	33.52	[29.98 – 37.16]	10.72
Site B	9.24	[8.61 – 9.94]	7.15	14.46	[13.15 – 15.00]	6.38	22.52	[20.16 – 24.18]	8.93
Site C	11.24	[10.26 – 11.83]	6.98	16.44	[15.60 – 17.48]	5.73	28.02	[24.11 – 30.18]	10.83
Site D	10.34	[9.52 – 10.78]	6.10	15.04	[13.96 – 16.53]	8.53	24.85	[22.96 – 28.54]	11.22

Table A.2
a)–d) Percentile values and relative uncertainties of the photo data (*LVA*): Percentile values (D_{16}, D_{50}, D_{84}) and 95% confidence interval (CI) of the *LVA* (longest visible axis) from photo data of all sample sites. ***GAD***: Grid-approach, distorted photos; ***GAU***: Grid-approach, undistorted photos; ***RAD***: Random-approach, distorted photos; ***RAU***: Random-approach, undistorted photos.

A.2a

Photo *LVA* (*GAD*)	D_{16} [mm]	95% C.I. [mm]	ε_{16} [±%]	D_{50} [mm]	95% C.I. [mm]	ε_{50} [±%]	D_{84} [mm]	95% C.I. [mm]	ε_{84} [±%]
Site A	8.80	[7.84 – 10.93]	17.56	22.33	[19.94 – 27.72]	17.42	52.97	[45.12 – 60.48]	14.50
Site B	8.13	[6.60 – 9.13]	15.54	15.46	[13.84 – 16.80]	9.58	29.42	[26.03 – 33.54]	12.76
Site C	9.66	[8.22 – 10.72]	12.94	18.00	[16.63 – 20.59]	11.00	35.24	[30.07 – 41.95]	16.85
Site D	9.29	[7.45 – 11.07]	19.48	19.67	[17.36 – 22.42]	12.86	43.43	[35.79 – 48.38]	14.50

A.2b

Photo *LVA* (*GAU*)	D_{16} [mm]	95% C.I. [mm]	ε_{16} [±%]	D_{50} [mm]	95% C.I. [mm]	ε_{50} [±%]	D_{84} [mm]	95% C.I. [mm]	ε_{84} [±%]
Site A	10.66	[8.24 – 11.83]	16.84	21.59	[19.10 – 24.17]	11.74	46.67	[38.28 – 53.60]	16.42
Site B	8.32	[7.26 – 9.32]	12.40	16.01	[13.86 – 17.80]	12.31	30.33	[27.97 – 33.92]	9.81
Site C	8.66	[7.40 – 9.72]	13.40	19.41	[16.89 – 22.72]	15.02	37.14	[34.24 – 42.89]	11.65
Site D	9.33	[7.79 – 11.48]	19.77	20.23	[18.04 – 23.19]	12.73	39.89	[35.28 – 44.04]	10.99

A.2c

Photo *LVA* (*RAD*)	D_{16} [mm]	95% C.I. [mm]	ε_{16} [±%]	D_{50} [mm]	95% C.I. [mm]	ε_{50} [±%]	D_{84} [mm]	95% C.I. [mm]	ε_{84} [±%]
Site A	8.80	[7.52 – 12.11]	26.12	21.91	[19.56 – 25.86]	14.38	46.84	[38.02 – 52.13]	15.06
Site B	7.86	[6.87 – 9.17]	14.66	15.90	[14.02 – 17.39]	10.60	28.70	[25.69 – 35.35]	16.84
Site C	7.90	[6.34 – 10.32]	25.18	19.09	[15.93 – 22.73]	17.81	35.68	[33.19 – 39.86]	9.35
Site D	8.52	[6.46 – 10.74]	25.14	19.06	[16.91 – 21.17]	11.18	42.06	[35.48 – 46.45]	13.04

A.2d

Photo *LVA* (*RAU*)	D_{16} [mm]	95% C.I. [mm]	ε_{16} [±%]	D_{50} [mm]	95% C.I. [mm]	ε_{50} [±%]	D_{84} [mm]	95% C.I. [mm]	ε_{84} [±%]
Site A	8.64	[6.91 – 10.75]	22.23	23.67	[19.97 – 27.17]	15.21	51.63	[41.09 – 59.86]	18.17
Site B	7.15	[6.55 – 8.69]	14.90	14.35	[12.77 – 16.26]	12.18	25.02	[21.68 – 28.51]	13.64
Site C	7.25	[6.14 – 8.29]	14.81	15.88	[14.92 – 18.78]	12.14	35.61	[30.96 – 40.87]	13.91
Site D	7.42	[5.98 – 9.60]	24.37	19.89	[17.26 – 22.87]	14.10	42.13	[34.30 – 47.15]	15.25

Table A.3
a)–d) Percentile values and relative uncertainties of the photo data (*SVA*): Percentile values (D_{16}, D_{50}, D_{84}) and 95% confidence interval (CI) of the *SVA* (shortest visible axis) from photo data of all sample sites. ***GAD***: Grid-approach, distorted photos; ***GAU***: Grid-approach, undistorted photos; ***RAD***: Random-approach, distorted photos; ***RAU:*** Random-approach, undistorted photos.

A.3a

Photo *SVA* (*GAD*)	D_{16} [mm]	95% C.I. [mm]	$>\varepsilon_{16}$ [±%]	D_{50} [mm]	95% C.I. [mm]	$>\varepsilon_{50}$ [±%]	D_{84} [mm]	95% C.I. [mm]	$>\varepsilon^{84}$ [±%]
Site A	5.59	[4.87 – 7.07]	19.66	13.87	[11.83 – 16.52]	16.91	30.58	[25.60 – 36.49]	17.80
Site B	4.72	[4.17 – 5.81]	17.41	8.91	[8.30 – 9.89]	8.92	16.36	[14.44 – 20.82]	19.51
Site C	6.17	[4.86 – 6.68]	14.73	11.24	[9.93 – 12.66]	12.12	21.62	[19.20 – 26.05]	15.85
Site D	5.63	[5.03 – 6.41]	12.24	11.96	[10.88 – 13.43]	10.64	27.60	[23.68 – 29.86]	11.20

A.3b

Photo *SVA* (*GAU*)	D_{16} [mm]	95% C.I. [mm]	$>\varepsilon_{16}$ [±%]	D_{50} [mm]	95% C.I. [mm]	$>\varepsilon_{50}$ [±%]	D_{84} [mm]	95% C.I. [mm]	$>\varepsilon_{84}$ [±%]
Site A	6.07	[5.59 – 6.69]	9.03	12.24	[10.73 – 14.52]	15.48	27.53	[22.98 – 33.20]	18.56
Site B	5.15	[4.73 – 5.60]	8.48	9.60	[8.58 – 10.89]	12.03	18.97	[16.39 – 20.92]	11.92
Site C	5.13	[4.67 – 6.32]	16.03	11.80	[10.08 – 13.02]	12.46	24.50	[20.74 – 26.36]	11.46
Site D	5.62	[4.53 – 7.00]	21.97	11.44	[10.32 – 13.55]	14.12	25.37	[22.02 – 27.13]	10.05

A.3c

Photo *SVA* (*RAD*)	D_{16} [mm]	95% C.I. [mm]	$>\varepsilon_{16}$ [±%]	D_{50} [mm]	95% C.I. [mm]	$>\varepsilon_{50}$ [±%]	D_{84} [mm]	95% C.I. [mm]	$>\varepsilon_{84}$ [±%]
Site A	5.75	[4.96 – 7.34]	20.70	12.76	[11.50 – 14.80]	12.91	26.77	[23.12 – 33.53]	19.45
Site B	4.70	[4.35 – 5.11]	8.08	8.96	[8.04 – 10.32]	12.70	17.98	[15.80 – 20.48]	13.03
Site C	4.57	[3.78 – 5.58]	19.80	10.72	[9.41 – 12.18]	12.90	23.77	[20.52 – 27.35]	14.36
Site D	4.92	[3.43 – 6.50]	31.11	11.10	[9.66 – 11.79]	9.59	24.34	[20.22 – 27.93]	15.83

A.3d

Photo *SVA* (*RAU*)	D_{16} [mm]	95% C.I. [mm]	$>\varepsilon_{16}$ [±%]	D_{50} [mm]	95% C.I. [mm]	$>\varepsilon_{50}$ [±%]	D_{84} [mm]	95% C.I. [mm]	$>\varepsilon_{84}$ [±%]
Site A	5.43	[4.99 – 7.16]	19.93	12.48	[10.84 – 14.77]	15.75	27.36	[24.27 – 32.64]	15.30
Site B	4.42	[3.99 – 4.98]	11.14	8.26	[7.56 – 9.38]	11.01	15.92	[13.54 – 18.04]	14.15
Site C	4.46	[4.04 – 5.06]	11.45	10.17	[8.30 – 11.64]	16.45	21.96	[18.18 – 24.58]	14.57
Site D	4.82	[3.85 – 5.92]	21.42	11.66	[10.49 – 13.14]	11.37	26.03	[22.12 – 28.43]	12.11

Table A.4
Percentile values and relative uncertainties of the sieve data: Percentile values (D_{16}, D_{50}, D_{84}) and confidence range of ±5 percentiles of all sample sites from sieve data.

Sieve data ± 5 percentiles	D_{16} [mm]	$[D_{11} - D_{21}]$ [mm]	ε_{16} [±%]	D_{50} [mm]	$[D_{45} - D_{55}]$ [mm]	ε_{50} [±%]	D_{84} [mm]	$[D_{79} - D_{89}]$ [mm]	ε_{84} [±%]
Site A	10.86	[8.23 – 13.48]	24.18	35.41	[30.16 – 41.54]	16.07	102.12	[85.12 – 119.12]	16.65
Site B	7.63	[5.99 – 9.10]	20.41	17.89	[15.91 – 19.90]	11.15	31.89	[29.57 – 41.61]	18.89
Site C	6.33	[5.06 – 7.60]	19.99	15.88	[14.45 – 17.96]	11.07	30.33	[28.20 – 36.87]	14.30
Site D	8.02	[6.28 – 9.63]	20.88	19.69	[17.68 – 21.70]	10.22	39.12	[31.36 – 47.30]	20.36

Appendix B

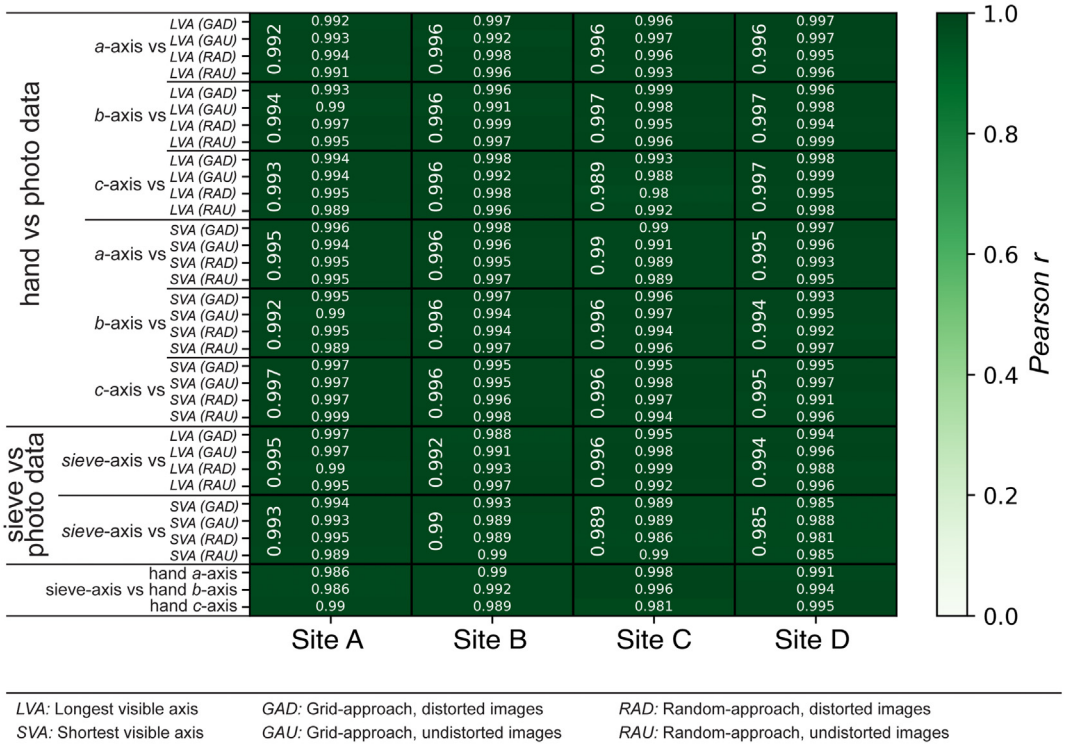

Fig. B.1. Pearson *r*-values: Colour-coded table of Pearson *r*-values and averages thereof (vertically oriented). Dark colours denote a good correlation (i.e., $r = 1.00$).

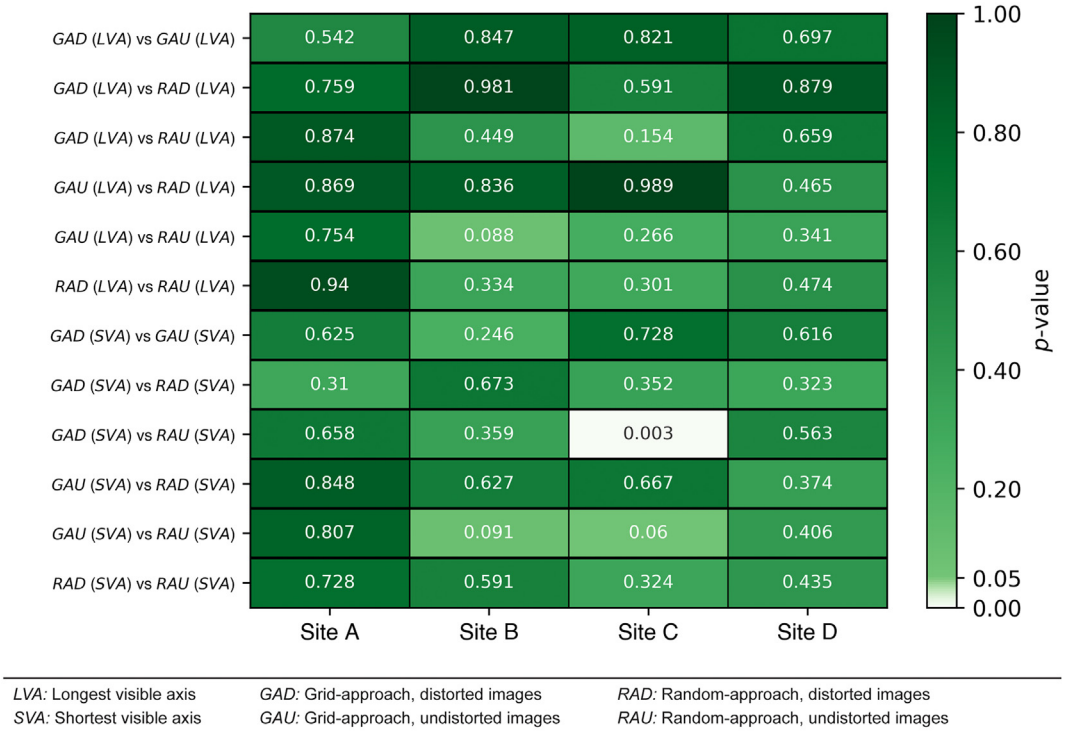

Fig. B.2. KS2 *p*-values of all photo acquisition approaches: Colour-coded *p*-values based on the KS2 test (Kolmogorov-Smirnov two-sample test; see methods) with an alpha level of 0.05. Dark colours denote a good correlation (i.e., *p*-value = 1.00), light colours show a poor correlation (*p*-value = 0.00).

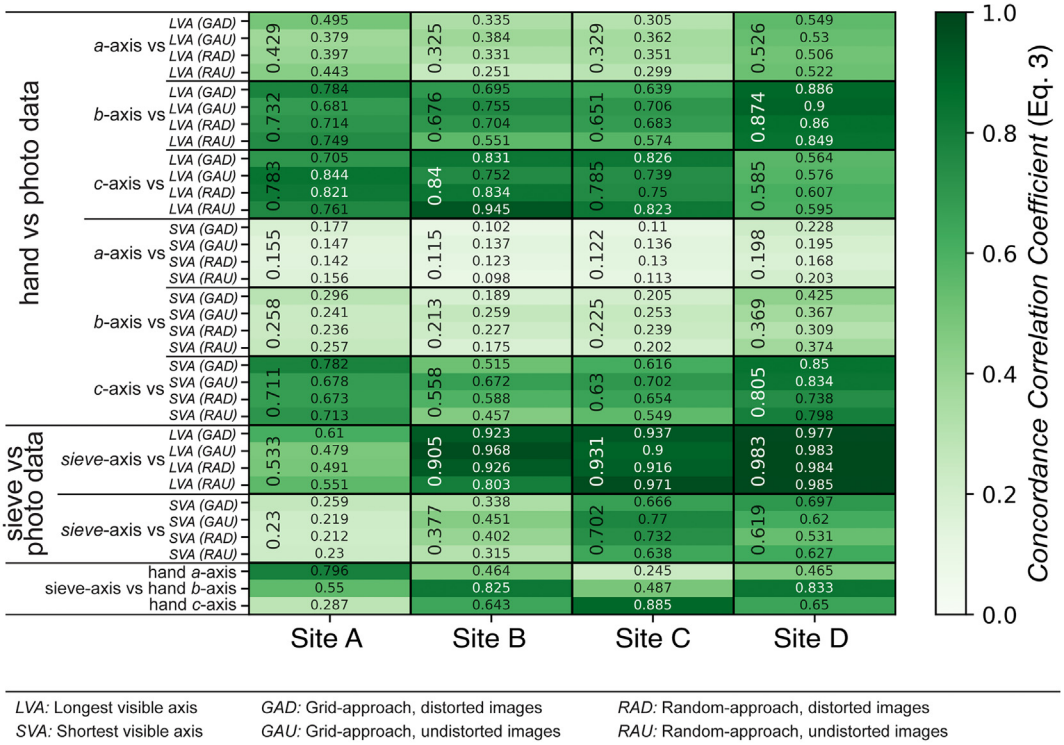

Fig. B.3. *CCC* values of the original datasets: Colour-coded *CCC* values (see methods) and averages thereof (vertically oriented) of the original datasets. Dark colours denote a good correlation (i.e., *CCC* = 1.00), light colours show a poor correlation (*CCC* = 0.00).

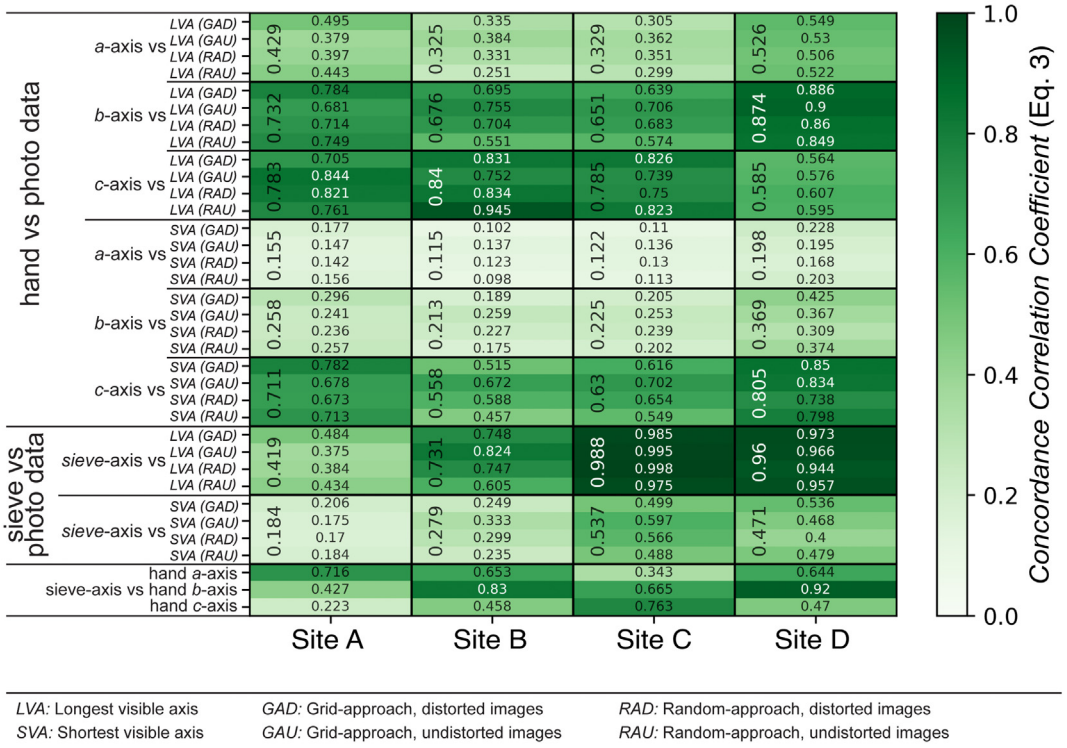

Fig. B.4. *CCC* values of corrected sieve datasets: Colour-coded *CCC* values (see methods) and averages thereof (vertically oriented) of the sieve data now corrected by a factor of *Ds*/hand-*b*-axis = 0.85. Dark colours denote a good correlation (i.e., *CCC* = 1.00), light colours show a poor correlation (*CCC* = 0.00).

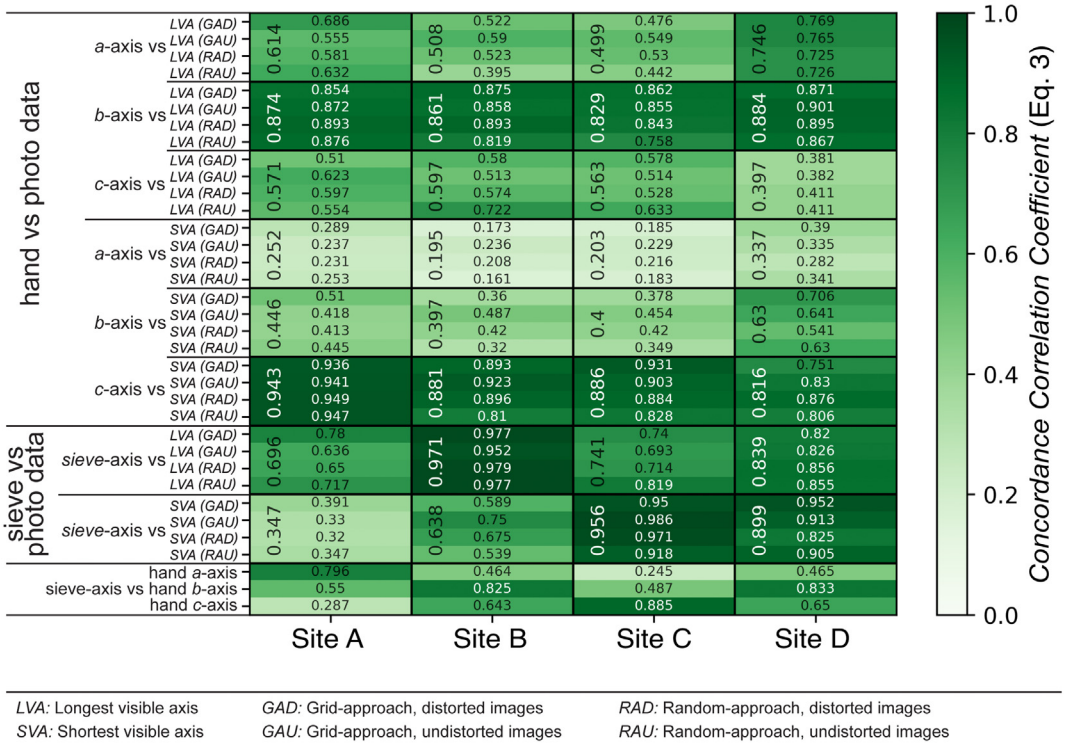

Fig. B.5. *CCC* values of corrected photo datasets: Colour-coded *CCC* values (see methods) and averages thereof (vertically oriented) of the photo data now corrected by a factor of *LVA*/hand-*b*-axis = 0.83 and *SVA*/hand-*c*-axis = 0.73. Dark colours denote a good correlation (i.e., *CCC* = 1.00), light colours show a poor correlation (*CCC* = 0.00).

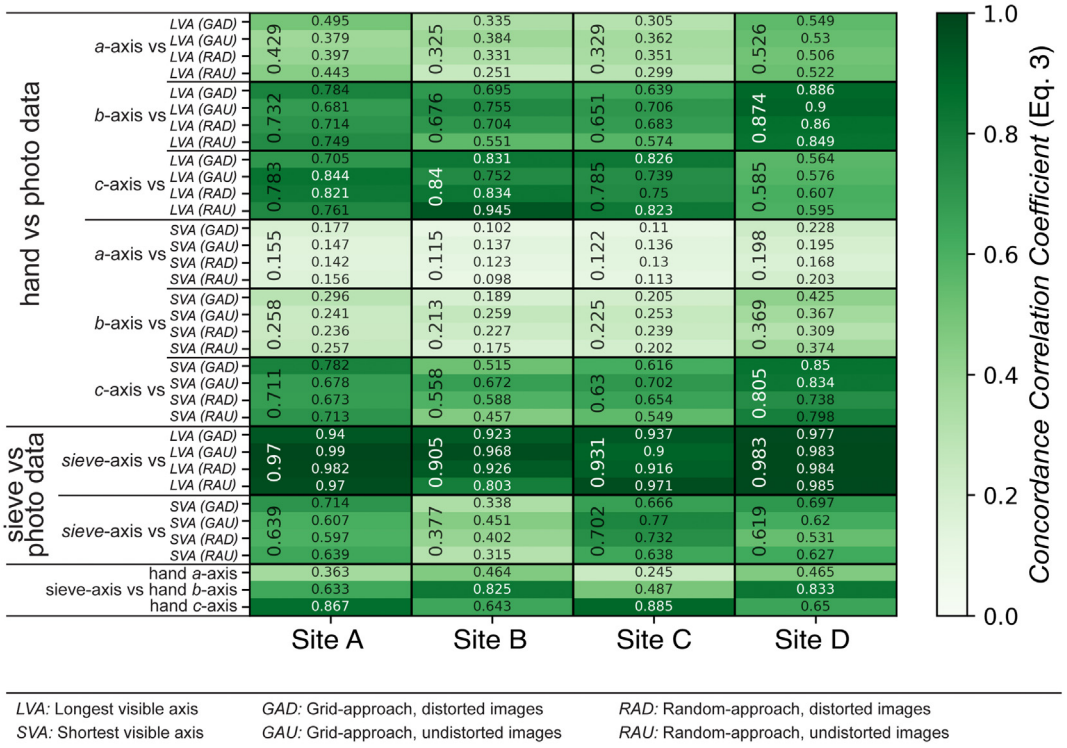

Fig. B.6. *CCC* of sieve data with grains >125 mm removed: Colour-coded *CCC* values (see methods) and averages thereof (vertically oriented) of the sieve data where grain sizes > 125 mm were removed from the dataset. Dark colours denote a good correlation (i.e., *CCC* = 1.00), light colours show a poor correlation (*CCC* = 0.00).

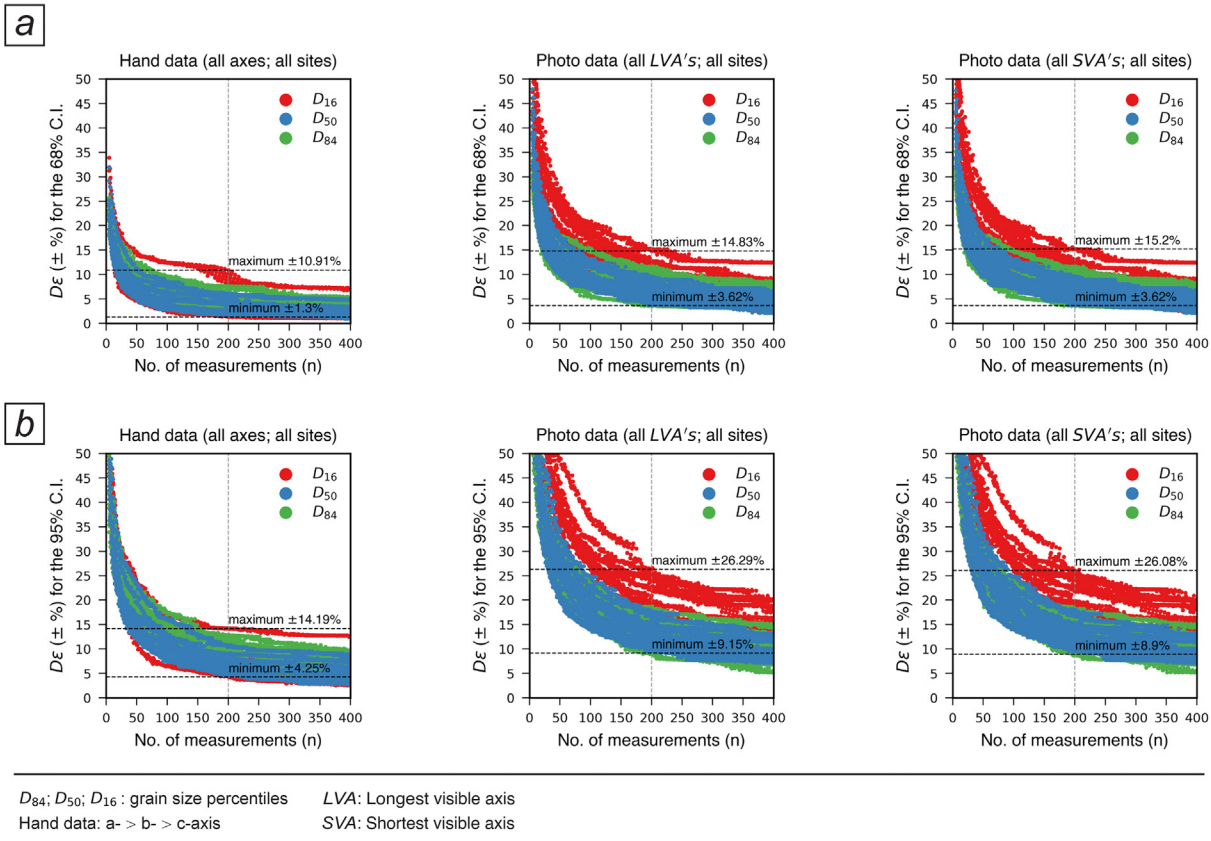

Fig. B.7. Uncertainties on the hand and photo data: Normalised percentile uncertainties (see methods) versus increasing number of measurements for a) the 68% confidence interval (CI) and b) the 95% CI. Vertical lines mark threshold for 200 measurements. Horizontal lines and related percent numbers denote the minimum and maximum uncertainty value per measuring method at n = 200, independent of the sample sites and percentiles.

Appendix C. Supplementary data

Supplementary data to this article can be found online at https://doi.org/10.1016/j.sedgeo.2023.106340.

References

Aberle, J., Nikora, V., 2006. Statistical properties of armored gravel bed surfaces. Water Resources Research 42, 1–11. https://doi.org/10.1029/2005WR004674.

Adams, J., 1979. Gravel size Analysis from Photographs. Journal of the Hydraulics Division 10, 1247–1255. https://doi.org/10.1002/9781118669709.ch15.

Altman, D.G., 1990. Practical Statistics for Medical Research. 1st edition. Chapman and Hall, New York https://doi.org/10.1201/9780429258589 (624 pp.).

Attal, M., Lavé, J., 2006. Changes of bedload characteristics along the Marsyandi River (central Nepal): Implications for understanding hillslope sediment supply, sediment load evolution along fluvial networks, and denudation in active orogenic belts. Geological Society of America 398, 143–171. https://doi.org/10.1130/2006.2398(09).

Attal, M., Mudd, S.M., Hurst, M.D., Weinman, B., Yoo, K., Naylor, M., 2015. Impact of change in erosion rate and landscape steepness on hillslope and fluvial sediments grain size in the Feather River basin (Sierra Nevada, California). Earth Surface Dynamics 3, 201–222. https://doi.org/10.5194/esurf-3-201-2015.

Batel, W., 1960. Die Korngrössenanalyse. Einführung in die Korngrössenmesstechnik. Verfahrenstechnik in Einzeldarstellungen8. Springer, Berlin, Heidelberg. https://doi.org/10.1007/978-3-662-01501-8_4 (156 pp.). (in German).

Blott, S.J., Pye, K., 2007. Particle shape: a review and new methods of characterization and classification. Sedimentology 55, 31–63. https://doi.org/10.1111/j.1365-3091.2007.00892.x.

Bradski, G., 2000. The OpenCV Library. Dr. Dobb's Journal of Software Tools 120, 122–125.

Brayshaw, A.C., 1984. Characteristics and origin of cluster bedforms in coarse-grained alluvial channels. In: Koster, E.H., Steel, R.J. (Eds.), Sedimentology of Gravels and Conglomerates. Canadian Society of Petroleum Geologists Memoir, pp. 77–85.

Bunte, K., Abt, S.R., 2001. Sampling surface and subsurface particle-size distributions in wadable gravel-and cobble-bed streams for analyses in sediment transport, hydraulics, and streambed monitoring. General Technical Report RMRS-GTR-74. U.S. Department of Agriculture, Forest Service, Rocky Mountain Research Station, Fort Collins, CO https://doi.org/10.2737/RMRS-GTR-74 (428 pp.).

Bürgisser, Heinz M., 1980. Zur Mittel-Miozänen Sedimentation im nordalpinen Molassebecken: Das "Appenzellergranit"-Leitniveau des Hörnli-Schuttfächers (OSM). Ph.D. ThesisETH Zurich, Switzerland https://doi.org/10.3929/ethz-a-000218245 (196 pp.). (in German).

Buscombe, D., 2008. Estimation of grain-size distributions and associated parameters from digital images of sediment. Sedimentary Geology 210, 1–10. https://doi.org/10.1016/j.sedgeo.2008.06.007.

Butler, J.B., Lane, S.N., Chandler, J.H., 2001. Automated extraction of grain-size data from gravel surfaces using digital image processing. Journal of Hydraulic Research 39, 519–529. https://doi.org/10.1080/00221686.2001.9628276.

Carbonneau, P.E., Bizzi, S., Marchetti, G., 2018. Robotic photosieving from low-cost multirotor sUAS : a proof-of-concept. Earth Surface Processes and Landforms 43, 1160–1166. https://doi.org/10.1002/esp.4298.

Chardon, V., Piasny, G., Schmitt, L., 2021. Comparison of software accuracy to estimate the bed grain size distribution from digital images: a test performed along the Rhine River. River Research and Applications 38, 358–367. https://doi.org/10.1002/rra.3910.

Church, M.A., 2006. Bed material transport and the morphology of alluvial river channels. Annual Review of Earth and Planetary Sciences 34, 325–354. https://doi.org/10.1146/annurev.earth.33.092203.122721.

Church, M.A., McLean, D.G., Wolcott, J.F., 1987. River bed gravels: sampling and analysis. In: Thorne, C.R., Bathurst, J.C., Hey, R.D. (Eds.), Sediment Transport in Gravel-Bed Rivers. John Wiley and Sons Ltd., Chichester, pp. 43–88.

Claude, A., Akçar, N., Ivy-Ochs, S., Schlunegger, F., Rentzel, P., Puempin, C., Tikhomirov, D., Kubik, P.W., Vockenhube, C., Dehnert, A., Rahn, M., Schlüchter, C., 2017. Chronology of Quaternary terrace deposits at the locality Hohle Gasse (Pratteln, NW Switzerland). Swiss Journal of Geosciences 110, 793–809. https://doi.org/10.1007/s00015-017-0278-z.

Dade, W.B., Friend, P.F., 1998. Grain-size, sediment-transport regime, and channel slope in alluvial rivers. Journal of Geology 106, 661–675. https://doi.org/10.1086/516052.

Daniels, M.D., McCusker, M.H., 2010. Operator bias characterizing stream substrates using Wolman pebble counts with a standard measurement template. Geomorphology 115, 194–198. https://doi.org/10.1016/j.geomorph.2009.09.038.

Detert, M., Weitbrecht, V., 2012. Automatic object detection to analyze the geometry of gravel grains – a free stand-alone tool. In: Muñoz, R.M. (Ed.), River Flow 2012: Proceedings of the International Conference on Fluvial Hydraulics. Taylor and Francis Group, London, pp. 595–600.

Diplas, P., Fripp, J.B., 1992. Properties of various sediment sampling procedures. Journal of Hydraulic Engineering, ASCE 118, 955–970. https://doi.org/10.1061/(ASCE)0733-9429(1992)118:7(955).

Duller, R.A., Whittaker, A.C., Fedele, J.J., Whitchurch, A.L., Springett, J., Smithells, R., Fordyce, S., Allen, P.A., 2010. From grain size to tectonics. Journal of Geophysical Research - Earth Surface 115, 1–19. https://doi.org/10.1029/2009JF001495.

Eaton, B.C., Dan Moore, R., Mackenzie, L.G., 2019. Percentile-based grain size distribution analysis tools (GSDtools)-estimating confidence limits and hypothesis tests for comparing two samples. Earth Surface Dynamics 7, 789–806. https://doi.org/10.5194/esurf-7-789-2019.

Ferguson, R.I., Paola, C., 1997. Bias and precision of percentiles of bulk grain size. Earth Surface Processes and Landforms 22, 1061–1077. https://doi.org/10.1002/(SICI)1096-9837(199711)22:11%3C1061::AID-ESP809%3E3.0.CO;2-L.

Fernlund, J.M.R., Zimmerman, R.W., Kragic, D., 2007. Influence of volume/mass on grain-size curves and conversion of image-analysis size to sieve size. Engineering Geology 90, 124–137. https://doi.org/10.1016/j.enggeo.2006.12.007.

Fripp, J.B., Diplas, P., 1993. Surface Sampling in Gravel Streams. Journal of Hydraulic Engineering 118, 473–490. https://doi.org/10.1061/(ASCE)0733-9429(1993)119:4(473).

Galia, T., Škarpich, V., Gajdošová, K., Krpec, P., 2017. Variability of Wolman pebble samples in gravel/cobble bed streams. Acta Scientiarum Polonorum-Formatio Circumiectus 16, 237–246. https://doi.org/10.15576/ASP.FC/2017.16.1.237.

Garefalakis, P., Schlunegger, F., 2018. Link between concentrations of sediment flux and deep crustal processes beneath the European Alps. Scientific Reports 8, 1–11. https://doi.org/10.1038/s41598-017-17182-8.

Graham, D.J., Reid, I., Rice, S.P., 2005a. Automated sizing of coarse-grained sediments: image-processing procedures. Mathematical Geology 37, 1–28. https://doi.org/10.1007/s11004-005-8745-x.

Graham, D.J., Rice, S.P., Reid, I., 2005b. A transferable method for the automated grain sizing of river gravels. Water Resources Research 41 (W07020), 1–12. https://doi.org/10.1029/2004WR003868.

Graham, D.J., Rollet, A.J., Piégay, H., Rice, S.P., 2010. Maximizing the accuracy of image-based surface sediment sampling techniques. Water Resources Research 46, 1–15. https://doi.org/10.1029/2008WR006940.

Green, J.C., 2003. The precision of sampling grain-size percentiles using the Wolman method. Earth Surface Processes and Landforms 28, 979–991. https://doi.org/10.1002/esp.513.

Guerit, L., Barrier, L., Liu, Y., Narteau, C., Lajeunesse, E., Gayer, E., Métivier, F., 2018. Uniform grain-size distribution in the active layer of a shallow, gravel-bedded, braided river (the Urumqi River, China) and implications for paleo-hydrology. Earth Surface Dynamics 6, 1011–1021. https://doi.org/10.5194/esurf-6-1011-2018.

Haldemann, E.G., 1948. Geologie des Schallenberg-Honegg-Gebietes (Oberes Emmental). Ph.D. ThesisUniversity of Bern, Switzerland (124 pp. in German).

Harvey, E.L., Hales, T.C., Hobley, D.E.J., Liu, J., Fan, X., 2022. Measuring the grain-size distributions of mass movement deposits. Earth Surface Processes and Landforms 47, 1599–1614. https://doi.org/10.1002/esp.5337.

Hey, R.D., 1979. Flow resistance in gravel-bed rivers. Journal of the Hydraulics Division, American Society of Civil Engineers 105, 365–379. https://doi.org/10.1061/JYCEAJ.0005178.

Hodges Jr., J.L., 1958. The significance Probability of the Smirnov Two-Sample Test. Arkiv för Matematik 3, 469–486. https://doi.org/10.1007/BF02589501.

Hoey, T.B., Ferguson, R., 1994. Numerical simulation of downstream fining by selective transport in gravel bed rivers: Model development and illustration. Water Resources Research 30, 2251–2260. https://doi.org/10.1029/94WR00556.

Ibbeken, H., Schleyer, R., 1986. Photo-sieving: a method for grain-size analysis of coarse-grained, unconsolidated bedding surfaces. Earth Surface Processes and Landforms 11, 59–77. https://doi.org/10.1002/esp.3290110108.

Inman, D.L., 1952. Measures for describing the size distribution of sediments. Journal of Sedimentary Petrology 22, 125–145. https://doi.org/10.1306/D42694DB-2B26-11D7-8648000102C1865D.

Johansson, C.E., 1976. Structural studies of frictional sediments. Geografiska Annaler. Series A, Physical Geography 58, 201–301. https://doi.org/10.1080/04353676.1976.11879939.

Kellerhals, R., Bray, D.I., 1971. Sampling procedures for coarse fluvial sediments. Journal of the Hydraulics Division 8, 1165–1180. https://doi.org/10.1061/JYCEAJ.0003044.

Kondolf, G.M., Li, S., 1992. The pebble count technique for quantifying surface bed material size in instream flow studies. Rivers 3, 80–87.

Lane, E.W., 1955. The importance of fluvial morphology in hydraulic engineering. Proceedings of the American Society of Civil Engineers 81, 1–17.

Leopold, L.B., 1970. An improved method for size distribution of stream bed gravel. Water Resources Research 6, 1357–1366. https://doi.org/10.1029/WR006i005p01357.

Leopold, L.B., 1992. Sediment size that determines channel morphology. Dynamics of Gravel-Bed Rivers 297–311.

Lin, L.I., 1989. A concordance correlation coefficient to evaluate reproducibility. Biometrics 45, 255–268. https://doi.org/10.2307/2532051.

Lin, L.I., 2000. A note on the concordance correlation coefficient. Biometrics 56, 324–325. https://doi.org/10.1111/j.0006-341X.2000.00324.x.

Litty, C., Schlunegger, F., 2017. Controls on pebbles' size and shape in streams of the Swiss Alps. The Journal of Geology 125, 101–112. https://doi.org/10.1086/689183.

Litty, C., Duller, R., Schlunegger, F., 2016. Paleohydraulic reconstruction of a 40 ka-old terrace sequence implies that water discharge was larger than today. Earth Surface Processes and Landforms 41, 884–898. https://doi.org/10.1002/esp.3872.

MacKenzie, L.G., Eaton, B.C., 2017. Large grains matter: contrasting bed stability and morphodynamics during two nearly identical experiments. Earth Surface Processes and Landforms 42, 1287–1295. https://doi.org/10.1002/esp.4122.

MacKenzie, L.G., Eaton, B.C., Church, M., 2018. Breaking from the average: why large grains matter in gravel-bed streams. Earth Surface Processes and Landforms 43, 3190–3196. https://doi.org/10.1002/esp.4465.

Mair, D., Do Prado, A.H., Garefalakis, P., Lechmann, A., Whittaker, A., Schlunegger, F., 2022. Grain size of fluvial gravel bars from close-range UAV imagery-uncertainty in

segmentation-based data. Earth Surface Dynamics 10, 953–973. https://doi.org/10.5194/esurf-2022-19.
Marchetti, G., Comiti, F., Bizzi, S., Belletti, B., Lastoria, B., Carbonneau, P.E., 2022. Mapping riverbed sediment size from Sentinel-2 satellite data. Earth Surface Processes and Landforms 47, 2544–2559. https://doi.org/10.1002/esp.5394.
Marcus, W.A., Ladd, S.C., Stoughton, J.A., Stock, J.W., 1995. Pebble counts and the role of user-dependent bias in documenting sediment size distributions. Water Resources Research 31, 2625–2631. https://doi.org/10.1029/95WR02171.
Meyer-Peter, E., Müller, R., 1948. Formulas for Bed-Load Transport. Proceedings of the 2nd meeting of the International Association of Hydraulic Research, Delft, pp. 39–64. http://resolver.tudelft.nl/uuid:4fda9b61-be28-4703-ab06-43cdc2a21bd7.
Mosley, M.P., Tindale, D.S., 1985. Sediment variability and bed material sampling in gravel-bed rivers. Earth Surface Processes and Landforms 10, 465–482. https://doi.org/10.1002/esp.3290100506.
Nemec, W., Porebski, S.J., Steel, R.J., 1980. Texture and structure of resedimented conglomerates: examples from Ksiaz Formation (Famenian–Tournaisian), southwestern Poland. Sedimentology 27, 519–538. https://doi.org/10.1111/j.1365-3091.1980.tb01645.x.
Neumann-Mahlkau, P., 1967. Korngrössenanalyse Grobklastischer Sedimente mit Hilfe von Aufschluss-Photographien. Sedimentology 9, 245–261. https://doi.org/10.1111/j.1365-3091.1967.tb02040.x. (in German).
Paola, C., Mohrig, D., 1996. Palaeohydraulics revisited: palaeoslope estimation in coarse-grained braided rivers. Basin Research 8, 243–254. https://doi.org/10.1046/j.1365-2117.1996.00253.x.
Parker, G., 1978. Self-formed straight rivers with equilibrium banks and mobile bed. Part 2. The gravel river. Journal of Fluid Mechanics 89, 127–146. https://doi.org/10.1017/S0022112078002505.
Parker, G., 1990. Surface-based bedload transport relation for gravel rivers. Journal of Hydraulic Research 28, 417–436. https://doi.org/10.1080/00221689009499058.
Petit, F., Houbrechts, G., Peeters, A., Hallot, E., Van Campenhout, J., Denis, A.C., 2015. Dimensionless critical shear stress in gravel-bed rivers. Geomorphology 250, 308–320. https://doi.org/10.1016/j.geomorph.2015.09.008.
Pfander, J., Schlunegger, F., Serra, E., Gribenski, N., Garefalakis, P., Akçar, N., 2022. Glaciofluvial sequences recording the Birrfeld Glaciation (MIS 5d–2) in the Bern area, Swiss Plateau. Swiss Journal of Geosciences 115, 1–24. https://doi.org/10.1186/s00015-022-00414-z.
Preusser, F., Büschelberger, M., Kemna, H.A., Miocic, J., Mueller, D., May, J.-H., 2021. Exploring possible links between Quaternary aggradation in the Upper Rhine Graben and the glaciation history of northern Switzerland. International Journal of Earth Sciences 110, 1827–1846. https://doi.org/10.1007/s00531-021-02043-7.
Purinton, B., Bookhagen, B., 2019. Introducing PebbleCounts: a grain-sizing tool for photo surveys of dynamic gravel-bed rivers. Earth Surface Dynamics 7, 859–877. https://doi.org/10.5194/esurf-7-859-2019.
Purinton, B., Bookhagen, B., 2021. Tracking downstream variability in large grain-size distributions in the south-central Andes. Journal of Geophysical Research - Earth Surface 126, 1–29. https://doi.org/10.1029/2021JF006260.
Rasband, W.S., 1997-2018. ImageJ. U. S. National Institutes of Health, Bethesda, Maryland, USA. https://imagej.nih.gov/ij/.
Recking, A., 2010. A comparison between flume and field bed load transport data and consequences for surface-based bed load transport prediction. Water Resources Research 46, 1–16. https://doi.org/10.1029/2009WR008007.
Recking, A., 2013. Simple method for calculating reach-averaged bed-load transport. Journal of Hydraulic Engineering 139, 70–75. https://doi.org/10.1061/(asce)hy.1943-7900.0000653.
Rice, S., Church, M., 1996. Sampling surficial fluvial gravels; the precision of size distribution percentile sediments. Journal of Sedimentary Research 66, 654–665. https://doi.org/10.2110/jsr.66.654.
Rice, S.P., Church, M., 2010. Grain-size sorting within river bars in relation to downstream fining along a wandering channel. Sedimentology 57, 232–251. https://doi.org/10.1111/j.1365-3091.2009.01108.x.
Ritter, J.R., Helley, E.J., 1969. Optical method for determining particle sizes of coarse sediment. Techniques of Water-Resources Investigations of the U.S. Geological Survey 5, 33. https://doi.org/10.3133/twri05C3.
Schlunegger, F., Delunel, R., Garefalakis, P., 2020. Short communication: field data reveal that the transport probability of clasts in Peruvian and Swiss streams mainly depends on the sorting of the grains. Earth Surface Dynamics 8, 717–728. https://doi.org/10.5194/esurf-8-717-2020.
Smith, Z.D., Maxwell, D.J., 2021. Constructing vertical measurement logs using UAV-based photogrammetry: applications for multiscale high-resolution analysis of coarse-grained volcaniclastic stratigraphy. Journal of Volcanology and Geothermal Research 409 (107122), 1–20. https://doi.org/10.1016/j.jvolgeores.2020.107122.
Stähly, S., Friedrich, H., Detert, M., 2017. Size ratio of fluvial grains' intermediate axes assessed by image processing and square-hole sieving. Journal of Hydraulic Engineering 143, 1–6. https://doi.org/10.1061/(ASCE)HY.1943-7900.0001286.
Storz-Peretz, Y., Laronne, J.B., 2013. Automatic grain sizing of vertical exposures of gravelly deposits. Sedimentary Geology 294, 13–26. https://doi.org/10.1016/j.sedgeo.2013.05.004.
Strom, K.B., Kuhns, R.D., Lucas, H.J., 2010. Comparison of automated image-based grain sizing to standard pebble-count methods. Journal of Hydraulic Engineering 136, 461–473. https://doi.org/10.1061/(ASCE)HY.1943-7900.0000198.
Tanner, H., 1944. Beitrag zur Geologie der Molasse zwischen Ricken und Hörnli. Mitteilungen der Thurgauischen Naturforschenden Gesellschaft 33, 1–108 (in German).
Wadell, H., 1936. Volume, shape, and shape position of rock fragments in openwork gravel. Geografiska Annaler 18, 74–92. https://doi.org/10.1080/20014422.1936.11880607.
Warrick, J.A., Rubin, D.M., Ruggiero, P., Harney, J.N., Draut, A.E., Buscombe, D., 2009. Cobble cam: grain-size-measurements of sand to boulder from digital photographs and autocorrelation analyses. Earth Surface Processes and Landforms 34, 155–161. https://doi.org/10.1002/esp.1877.
Watkins, S.E., Whittaker, A.C., Bell, R.E., Brooke, S.A.S., Ganti, V., Gawthorpe, R.L., Nixon, C. W., 2020. Straight from the source's mouth: Controls on field-constrained sediment export across the entire active Corinth Rift, central Greece. Basin Research 32, 1600–1625. https://doi.org/10.1111/bre.12444.
Wentworth, C.K., 1922. A scale of grade and class terms for clastic sediments. The Journal of Geology 30, 377–392. https://doi.org/10.1086/622910.
Whittaker, A.C., Duller, R.A., Springett, J., Smithells, R.A., Whitchurch, A.L., Allen, P.A., 2011. Decoding downstream trends in stratigraphic grain size as a function of tectonic subsidence and sediment supply. Geological Society of America Bulletin 7, 1363–1382. https://doi.org/10.1130/B30351.1.
Wilcock, P.R., McArdell, B.W., 1993. Surface-based fractional transport rates: mobilization thresholds and partial transport of sand-gravel sediments. Water Resources Research 29, 1297–1312. https://doi.org/10.1029/92WR02748.
Wohl, E.E., Anthony, D.J., Madsen, S.W., Thompson, D.M., 1996. A comparison of surface sampling methods for coarse fluvial sediments. Water Resources Research 32, 3219–3226. https://doi.org/10.1029/96WR01527.
Wolman, M.G., 1954. A method of sampling coarse river-bed material. EOS. Transactions of the American Geophysical Union 35, 951–956. https://doi.org/10.1029/TR035i006p00951.
Wong, M., Parker, G., 2006. Reanalysis and correction of bed-load relation of Meyer-Peter and Müller using their own database. Journal of Hydraulic Engineering 132, 1159–1168. https://doi.org/10.1061/(asce)0733-9429(2006)132:11(1159).
Woodget, A.S., Fyffe, C., Carbonneau, P.E., 2018. From manned to unmanned aircraft: Adapting airborne particle size mapping methodologies to the characteristics of sUAS and SfM. Earth Surface Processes and Landforms 43, 857–870. https://doi.org/10.1002/esp.4285.
Yuzyk, T.R., Winkler, T., 1991. Procedures for Bed-Material Sampling. Lesson Package No. 28. Environment Canada, Water Resources Branch, Sediment Survey Section, Ottawa, Canada, p. 100.
Zhang, Z., 2000. A flexible new technique for camera calibration. Technical Report MSR-TR-98-71. Microsoft Research, Microsoft Corporation. IEEE Transactions on Pattern Analysis and Machine Intelligence 22, 1330–1334. https://doi.org/10.1109/34.888718.
Zingg, T., 1935. Beitrag zur Schotteranalyse. Ph.D. ThesisSchweizerische mineralogische und petrographische Mitteilungen. 15. ETH Zurich, Switzerland, pp. 39–140. https://doi.org/10.3929/ethz-a-000103455 pp. 140. (in German).